IEEE Open Journal of
Power Electronics

Received 22 January 2024; revised 2 May 2024; accepted 21 May 2024. Date of publication 24 May 2024;
date of current version 12 June 2024. The review of this article was arranged by Associate Editor Rongwu Zhu.

Digital Object Identifier 10.1109/OJPEL.2024.3404954

Improvements to Real-Time Synchronization and Detection for a Dual-Active, Secondary-Driven Dynamic Wireless Power Transfer System

MATTHEW J HANSEN (Graduate Student Member, IEEE), AZMEER ZAHID (Graduate Student Member, IEEE), AND ABHILASH KAMINENI (Member, IEEE)

Department of Electrical and Computer Engineering, Utah State University, Logan, UT 84322 USA

CORRESPONDING AUTHOR: MATTHEW J HANSEN (e-mail: matthew.hansen@usu.edu)

This work was supported in part by the Advancing Sustainability through Powered Infrastructure for Roadway Electrification (ASPIRE) Center, an NSF ERC, under Award 1941524, and in part by the Utah State University College of Engineering.

ABSTRACT A novel control scheme applicable to in-road inductive wireless charging pads in a dynamic system is presented. Primary inverter current sensing allows the primary pad to detect an approaching secondary pad. Zero-crossing detection of the same current allows the primary to synchronize to the secondary, functioning as a synchronous inverter with dual-active switching. Such primary synchronous inverters allow for independent primary pads. Necessary measures to ensure stable operation of the design are discussed. The control scheme only adds an analog filter to the bare-bones open-loop design. The design is validated through simulation and hardware experimentation, with a strong demonstration of robustness.

INDEX TERMS Electric vehicles, inductive charging, inverters, power conversion, resonant converters, vehicle detection.

I. INTRODUCTION

Dynamic wireless power transfer (DWPT) in electric vehicles could increase the feasibility of vehicle electrification, potentially resulting in many environmental advantages. By electrifying a small portion of roadways, a majority of routes could be covered by electric vehicles (EVs) without stopping to recharge [1]. Although battery technology, modeling, and use optimization are improving [2], [3], [4] and novel battery charging solutions are being explored [5], [6], [7], battery limitations remain a weakness of EVs. With en-route, no-time-added charging through DWPT, electric vehicles could overcome two of the main weaknesses in a battery-centered approach to vehicle electrification: range anxiety and battery cost [8], [9]. The suitability of WPT for electric vehicles has been well-studied [10]. This paper further develops the real-time synchronization and detection, or synchronous inversion approach initially introduced in [11], [12], which in turn was an extension of the work in [13]. In comparison with [11], [12], the present paper includes a more rigorous proof of closed-loop stability, more thorough development of the underlying theory, and, as a proof of the maturity of the principles already presented in a conference paper, this sequel also describes a hardware demonstration of the operating principle at 15 kW.

Near-field wireless power transfer (WPT) is accomplished either through an electric field (capacitive power transfer, CPT) or a magnetic field (inductive power transfer, IPT). Although work in capacitive transfer shows promise [14], [15], [16], CPT still has limitations in air gap length and frequency that restrict the applicability of CPT to DWPT [17]. Most research on high-powered WPT for EVs uses IPT.

Work on stationary WPT has demonstrated the advantages of a bidirectional system, where the vehicle rectifier is active and therefore reversible [18]. We assume such an active rectifier on the secondary in the present work, which requires primary–secondary synchronization — a critical contribution of this work. In [18], [19], [20], control schemes have been developed to regulate power transfer on the secondary side

of a WPT system. In [21], and [22], the control scheme is designed to ensure low-loss zero-volt switching. The work in [23] provides an accurate method to measure energy transferred, which is an essential step in the commercialization of WPT for EVs. In [24], a framework for stationary charging with rotating magnetic fields and less ferrite is presented. The work in [25] provides a framework for overcoming large air gaps, which could be present in DWPT. Additionally, the work in [27] describes a method to assist a vehicle operator in achieving optimal alignment. Vehicle alignment is a critical enabling technology for DWPT, and any DWPT system must tolerate varying loads due to vehicle misalignment, but other works have treated vehicle alignment sufficiently. The extensive research environment around stationary WPT complements and enriches the present work while highlighting the need to extend those advances to DWPT with a robust and simple detection and synchronization scheme.

Beyond those general contributions to WPT, existing work describes how an in-road primary coil in a DWPT system can detect an approaching vehicle-mounted secondary coil. The approach in [26] accomplished synchronization with dedicated detection hardware, relying on ultrasonic sensors to detect the secondary. Such an approach is too slow and insufficiently robust for high-speed DWPT, including in-motion EV applications. Other work uses extra coils to detect approaching vehicles [27], [28], sensing current induced in an auxiliary coil to infer the proximity of a vehicle. This approach is fast and reliable enough to achieve DWPT but increases complexity and cost by requiring additional components. Continued advancement in DWPT technology requires a faster, simpler, and more reliable paradigm, one that does not require any additional bulky components and is as robust as the power transfer link itself. The proposed scheme achieves those objectives, demonstrating improvement over the current state-of-the-art. In [13], a robust, fast detection scheme is presented without relying on additional detection hardware, but the parasitic losses in the approach require constant pulsing and sampling, increasing system complexity and making each primary pad dependent on the preceding primary pad operation. In [13], [26], [28], all primary pads need a central synchronization signal, decreasing modularity and robustness. One advantage of approaches found in the literature body is their general applicability to various compensation topologies. The approach here, while potentially adaptable to other control schemes, assumes an LCCL topology.

The LCCL topology, visualized in Fig. 1, is among the commonly used approaches in WPT [13], [21], [22], [29], [30], in part due to a few key advantages. Unlike simple series compensation, the system can be perfectly tuned and operated with no load. Unlike basic parallel compensation, the LCCL system can achieve ZVS when perfectly tuned [30]. Finally, as discussed in [13], the inverter current and voltage are decoupled; more analysis of this decoupling is addressed in this paper. Although this approach may extend to other compensation topologies, this work assumes an LCCL system, or a coil with LCC compensation of the transmitter coil.

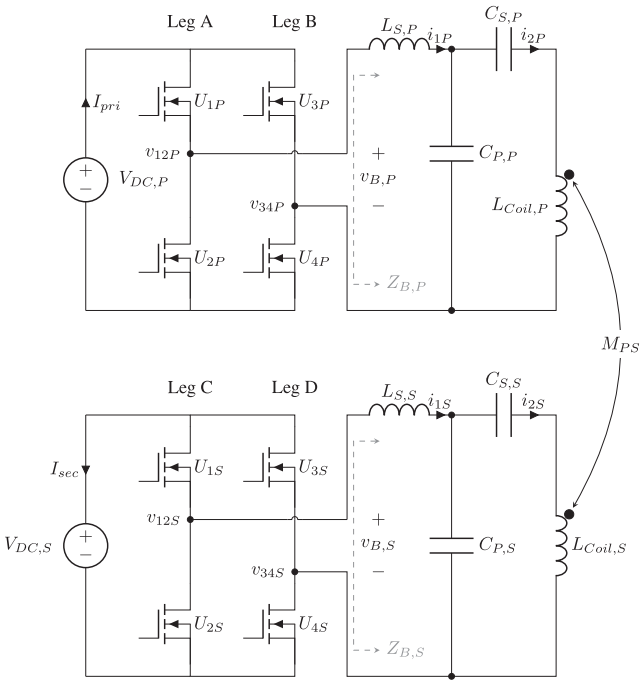

FIGURE 1. System overview of primary and secondary pad architectures with LCC compensation.

Recently, the concept of self-excited parity-time (PT) symmetry has emerged within WPT systems [31], [32]. Analysis of the PT-WPT system using coupled-mode theory (CMT) reveals that when the system is in the PT-symmetric region, the output load power and transmission efficiency are not influenced by changes in the coupling coefficient, which is typically not the case in LCC-compensated WPT systems [33]. Since the output power and transmission efficiency are invariant to the coupling efficiency, the PT-symmetric WPT system will be very useful for DWPT systems where misalignment is a major concern [34]. However, these systems suffer from the fact that the output power cannot be adjusted and hence require active control of the switches by synchronizing with the secondary side [33]. The control law and stability analysis presented in this paper can be effectively extended to a PT-WPT system to actively control the switches by synchronizing with the primary inverter current using zero-crossing detection.

The contributions of this paper are expansions of previous research in six critical directions. First, the design simplifies the approach in [13] by allowing a single control law for the primary and open-loop control for the secondary, using one threshold to determine both turn-on and turn-off. Second, in this approach, the primary coils are activated by the secondary, rather than neighboring primary pads. The result is that the secondary can initiate and cease power transfer, as necessary. The third improvement over the previous work is a simplified primary controller with no switching clock; the primary switching is driven by a simple comparator and adapts to the frequency and phase of the secondary. In the future, this

innovation could allow a secondary-based frequency-modulated controller that achieves ZVS with no required communication to the primary; removing the primary switching clock simplifies the primary control and eliminates a point of failure. All three of those innovations are implemented without a dedicated primary–secondary communication link or auxiliary coils, increasing system simplicity and robustness.

Those three innovations are discussed lightly in [11], [12], although this work presents a more thorough analysis than in [11], [12]. Compared to [11], [12], this work also includes three new and essential contributions. The first is the rigorous development of stability criteria, with analytical treatment of the nonlinear system components. The second new contribution is the consideration of imperfectly-tuned systems. The final difference between this discussion and the earlier, theoretical contributions of [11], [12] is a proof of concept through a 15 kW system.

This paper is organized as follows. Section II introduces pertinent characteristics of an LCCL WPT topology and introduces the basic concept, detailing how synchronous inversion on the primary can simplify the synchronization and detection operations. Section III presents practical considerations for implementing the system in a dynamic setting, including a discussion on stability. Section V demonstrates the effectiveness of the scheme through software simulation; Section VI mirrors Section V with hardware validation. A conclusion and discussion of potential impacts follow in Section VII. Appendix A works out the modeling of the nonlinear zero-crossing detector, and Appendix B proves stability in the time domain.

II. WPT IN A WELL-TUNED LCCL SYSTEM AND BASIC CONTROL SCHEME

The work presented here expands on previous work [11], [12], [13]. As in those works, this paper assumes an LCCL topology on both the primary and secondary side, although the control scheme could be adapted to other topologies as well. Quantities relevant to this discussion are defined in Table 1 and noted in Fig. 1. The notation for phasors, small-signal, DC, and large-signal quantities shown in Table 1 holds for all quantities. In the present system, the H-bridge switches at a fundamental frequency $f_f = 85$ kHz, in line with SAE J2954 standards. This section gives some essential background on LCCL systems in Section II-A, and describes the essential principle of operation in Section II-B.

A. WPT IN A WELL-TUNED LCCL SYSTEM

In a well-tuned LCCL system operating at $f_f = \omega_f/2\pi$, the magnitude of the impedance of each branch in either the primary or secondary (X_P and X_S, respectively) are given by

$$X_P = \left(\omega_f L_{S,P}\right) = \left(\frac{1}{\omega_f C_{P,P}}\right) = \left(\omega_f L_{Coil,P} - \frac{1}{\omega_f C_{S,P}}\right) \tag{1a}$$

TABLE 1. Referenced Quantities in an LCCL System

Phasor	Complete Signal	Small Signal	Value
$\bar{V}_{B,P}$	$v_{B,P}$	$\hat{v}_{B,P}$	Primary bridge voltage
$\bar{V}_{B,S}$	$v_{B,S}$	$\hat{v}_{B,S}$	Secondary bridge voltage
$\bar{I}_{1P}$	i_{1P}	$\hat{i}_{1P}$	Primary inverter current
$\bar{I}_{1S}$	i_{1S}	$\hat{i}_{1S}$	Secondary inverter current
X_P			Primary branch impedance (1a)
X_S			Secondary branch impedance (1b)
$V_{DC,P}$			Primary DC voltage
$V_{DC,S}$			Secondary DC voltage
I_{pri}			Primary DC bus current
I_{sec}			Secondary DC bus current
M_{PS}			Primary–secondary mutual inductance
f_f			Switching frequency
f_{z1}, f_{z2}			Primary natural response frequencies
f_{coil}			Resonant frequency of $L_{Coil,P}$ and $C_{S,P}$
$Z_{B,P}$			Output impedance seen by the primary inverter
f_{e1}, f_{e2}			Equilibrium frequencies of primary network and anti-resonance filter

$$X_S = \left(\omega_f L_{S,S}\right) = \left(\frac{1}{\omega_f C_{P,S}}\right) = \left(\omega_f L_{Coil,S} - \frac{1}{\omega_f C_{S,S}}\right) \tag{1b}$$

A brief explanation of the current–voltage decoupling phenomenon is given here. Consider the following equations defined by Kirchhoff's Voltage Law, where the total voltage around is calculated for each loop in Fig. 1:

$$\bar{V}_{B,P} = \left(-jX_P\right)\left(-\bar{I}_{2P}\right) \tag{2a}$$

$$j\omega_f M_{PS}\bar{I}_{2S} = \left(-jX_P\right)\left(\bar{I}_{1P}\right) \tag{2b}$$

$$j\omega_f M_{PS}\bar{I}_{2P} = \left(-jX_S\right)\left(\bar{I}_{1S}\right) \tag{2c}$$

$$\bar{V}_{B,S} = \left(-jX_S\right)\left(-\bar{I}_{2S}\right) \tag{2d}$$

Note that neither of the currents in (2a) and (2c) appear in (2b) and (2d), showing two decoupled systems. By solving the expressions in (2) for $\bar{I}_{1P}$ and $\bar{I}_{1S}$, we arrive at the expressions

$$\bar{I}_{1P} = \frac{j\omega_f M_{PS}\bar{V}_{B,S}}{X_S X_P} \tag{3a}$$

$$\bar{I}_{1S} = \frac{j\omega_f M_{PS}\bar{V}_{B,P}}{X_S X_P} \tag{3b}$$

As consequence of (3), $\bar{V}_{B,P}$ will not contribute to $\bar{I}_{1P}$, making the two quantities independent. The bridge impedance at

f_f approaches infinity, implying that any small-signal change to $v_{B,P}$ at f_f will not affect i_{1P}

The analysis conducted here assumes a well-tuned system. While variations in system parameters may admit some mistuning, as long as the current $\bar{I}_{1P}$ is largely induced by $\bar{V}_{B,S}$, not $\bar{V}_{B,P}$, the essential principle holds.

B. BASIC CONTROL SCHEME

The characteristics of the LCCL WPT topology described here allow for a simplified detection/synchronization scheme through synchronous inversion. Because power is transferred at the fundamental frequency f_f, we neglect higher harmonics. In synchronous rectification, the current and voltage of the fundamental harmonic are aligned such that $\angle\bar{V}_{B,S} = \angle\bar{I}_{1S} \pm 180\,^\circ$, forcing the secondary to act as a load. Synchronous inversion is the complement; $\angle\bar{V}_{B,P} = \angle\bar{I}_{1SP}$, forcing the primary to act as a power source. The trigger signal for each primary switching event is a zero crossing if the current i_{1P}, or a filtered version thereof. The trigger signal to begin primary commutating at all is $\bar{I}_{1P}$ exceeding some threshold. Noting the decoupling between the voltage and current in (3a), the voltage and current can be aligned. This is synchronous inversion, the central thesis of this work. The remainder of this section details how synchronous inversion can be used to simplify and increase robustness in detection and synchronization. Because synchronous inversion injects power into a system, which tends to be unstable, some practical considerations for stable operation are made in Section III.

The present approach uses inherent characteristics of the WPT current waveforms to replace any other primary–secondary communication links, as all information necessary for primary control in the dual-active system is contained in the $\bar{I}_{1P}$ current.

1) SECONDARY OPERATION

The secondary H-bridge operates in two modes, as a synchronous rectifier and as an inverter. The active switching allows some flexibility between the two modes. Given the voltage $\bar{V}_{B,S}$ and current$\bar{I}_{1S}$ defined in Fig. 1, it is defined that when

$$\Re\left(\bar{V}_{B,S}\bar{I}_{1S}^{*}\right) > 0, \tag{4}$$

the H-bridge is considered to be operating as an inverter, as in Fig. 2. Conversely, when

$$\Re\left(\bar{V}_{B,S}\bar{I}_{1S}^{*}\right) < 0, \tag{5}$$

the H-bridge is considered to be operating as a rectifier, as in Fig. 3. When the secondary is not coupled with a primary, then parasitic losses ensure that the condition in (4) is met. Because the voltage are current are decoupled as described in (3), the secondary can only change its mode by the application of a primary excitation. To request power, the secondary begins switching, which induces a signal on any coupled primary. After the secondary begins switching, but before primary–secondary coupling, the secondary-side H-bridge operates as an inverter, supplying only enough real current to counteract

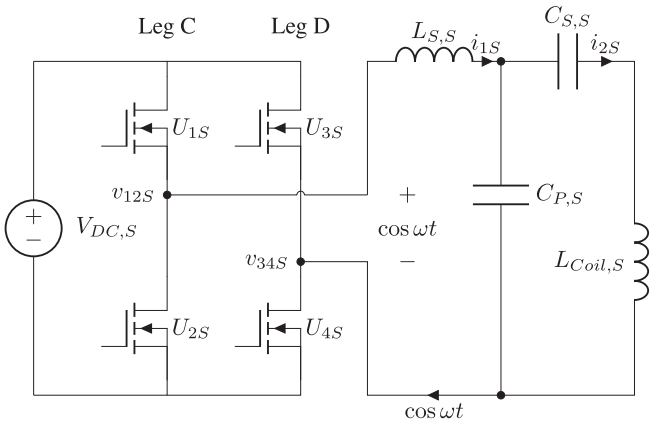

FIGURE 2. Diagram of secondary operating in inverter mode. Note that the current and phase are referenced as a power supply, and the $\Re(\bar{V}_{B,S}\bar{I}_{1S}^{*}) > 0$. Therefore, the secondary is transmitting power.

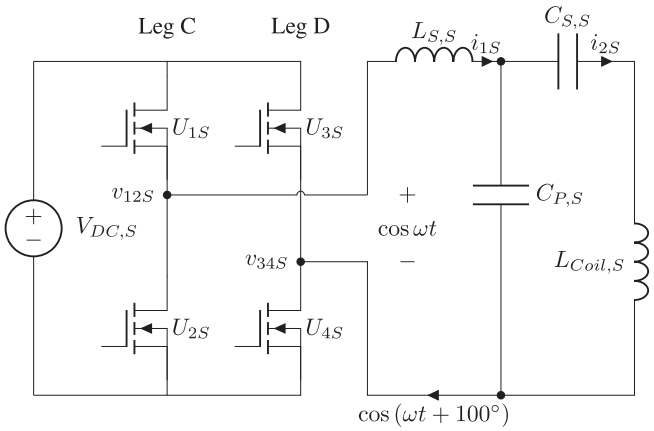

FIGURE 3. Diagram of secondary operating in rectifier mode. Note that the current and phase are referenced as a power supply, but the $\Re(\bar{V}_{B,S}\bar{I}_{1S}^{*}) < 0$. Therefore, the secondary is receiving power.

parasitic losses. When coupled to a primary, the secondary side operates as an open-loop synchronous rectifier. For both modes, the switches operate at a fixed fundamental frequency, f_f. The only difference between the two modes is the current i_{1S} induced by the primary pad.

The secondary side H-bridge maintains the same operation independent of the primary, but when the primary side injects power into the system, the change in $\bar{I}_{1S}$ causes the secondary H-bridge to begin functioning as a synchronous rectifier, rather than as an inverter. Although the system is effective with open-loop control of the secondary, the secondary can also control the total power transferred through voltage or phase modulation without additional hardware [20], or through a cascaded DC–DC converter. Previous work describes power transfer control of a similar system through current regulation, which can be simplified and applied here to regulate power on the secondary [18]. Because secondary power regulation is addressed in other works, a rigorous discussion is omitted here.

2) PRIMARY OPERATION

Both the primary and secondary networks are tuned for the same f_f. The primary inverter measures i_{1P}; the magnitude of the current determines when a vehicle is approaching. The primary inverter then synchronizes to i_{1P}, sending power into the secondary network. Because the primary inverter voltage $v_{B,P}$ is synchronized to i_{1P}, the primary H-bridge operates as a synchronous inverter. A synchronous rectifier tends to pull whatever power is available from a network, which is generally stable or stabilizable [35], [36]. In contrast, basic synchronous inversion tends to inject power into the network however possible, including at a natural response frequency of the primary network, f_z; considerations to avoid this phenomenon are discussed in Section III. Note the distinction between the switching frequency f_f, where $L_{S,P}$ and $C_{P,P}$ resonate, and the resonant frequency f_z, where the entire primary network resonates.

Initially, the primary inverter idles in a passive mode where $v_{B,P} = 0$, caused by closing both low-side switches U_{2P} and U_{4P}. The approaching AC magnetic field from the secondary pad induces a current i_{1P}, which flows through the primary inverter as described in Section II-A.

The magnitude of I_{1P} can be used to detect an approaching vehicle. As seen in (3a), I_{1P} is proportional to M_{PS} and $V_{B,S}$. When $M_{PS} \neq 0$, power transfer is possible. When $V_{B,S} \neq 0$, the secondary requests power from the primary by applying a voltage at $v_{B,S}$. Thus, some threshold, $I_{1crit,P}$ can be set, such that when $|\bar{I}_{1P}| > \bar{I}_{1crit,P}$, the primary determines power transfer is both possible and desired and begins to switch its H-bridge. To ensure power transfer is achievable, the threshold should be set below the typical current induced by the secondary, i.e.,

$$I_{1crit,P} < \frac{4\omega_f V_{DC,S} M_{PS}}{\pi X_P X_S} \tag{6}$$

Effectively, this condition guarantees that power can be transmitted at any misalignment condition, provided that M_{PS} is sufficiently large given the $V_{DC,S}$ and the compensation reactances. As misalignment perpendicular to the direction of travel increases, the power transfer duration tends to be shortened. Beyond those general statements, further information on the misalignment tolerance is determined by the coil magnetics and is beyond the scope of the present work.

To avoid instability, $I_{1crit,P}$ should be sufficiently high that the induced current from a neighboring primary pad alone will not cause $I_{1P} > I_{1crit,P}$, which would result in system-level daisy-chain instability where a primary is activated by a neighboring primary, rather than a secondary. Where $V_{DC,P}$ is the maximum primary inverter voltage amplitude and M_{PP} is the maximum mutual inductance between neighboring primary pads, this is expressed as

$$I_{1crit,P} > \left| \frac{4\omega_f V_{DC,P} M_{PP}}{\pi X_P^2} \right|. \tag{7}$$

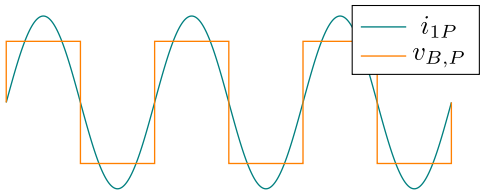

FIGURE 4. Sample figure of synchronous inversion in action. Note that the voltage commutes at the exact zero crossing, such that the sign of the voltage and current are always the same.

Two aspects of synchronization are relevant here. First, the primary H-bridge switching frequency needs to be synchronized to the secondary H-bridge switching frequency. Second, the phase of $\angle\bar{V}_{B,P}$ needs to be synchronized to the phase of $\angle\bar{I}_{1P}$. However, note that $|\bar{V}_{B,P}|$ and $|\bar{I}_{1P}|$ are irrelevant for synchronization. In effect, signal magnitude impacts detection, while signal phase impacts synchronization.

In the most simple case, the synchronization is accomplished by aligning the zero-crossings of $v_{B,P}$ with the zero-crossings of i_{1P}, or applying a positive voltage $v_{B,P}$ when a positive current i_{1P} is detected. We assume the angle between primary legs $\theta_{AB} = 180^\circ$, so the switches all commute on exactly the zero crossings of i_{1P}. Fig. 4 shows a sample switching action, with the voltage and current aligned. Synchronous inversion, in its most basic form, always injects power into the network. At f_f, the injected power will be pushed through the secondary's synchronous rectifier and to the load, and the current i_{1P} will be unaffected by the inverter voltage.

C. NOTE ON ROBUSTNESS

Synchronous inversion allows the secondary to initiate power transfer with a primary pad without any additional detection hardware. Both primary and secondary use active switching, which lowers losses. Moreover, external synchronization between neighboring primary pads becomes unnecessary, as the synchronization signal is an inherent property of power transfer and is always transmitted by the secondary during power transfer.

Several phenomena could potentially insert a phase shift into the system. However, any phase shift in the secondary will be matched by a phase shift in the primary, as demonstrated in Sections V and VI. Because the phase on a primary is always tied to the bridge current, the phase of the inverter will adapt in a dynamic system to send power. These features are all enabled over the wireless power transfer link, meaning that detection and synchronization will only fail when the power transfer itself fails. This approach increases the modularity and robustness of the system. As mentioned previously, the basic approach presented here tends to be unstable; slight modifications to the basic approach to guarantee stability are now detailed in Section III.

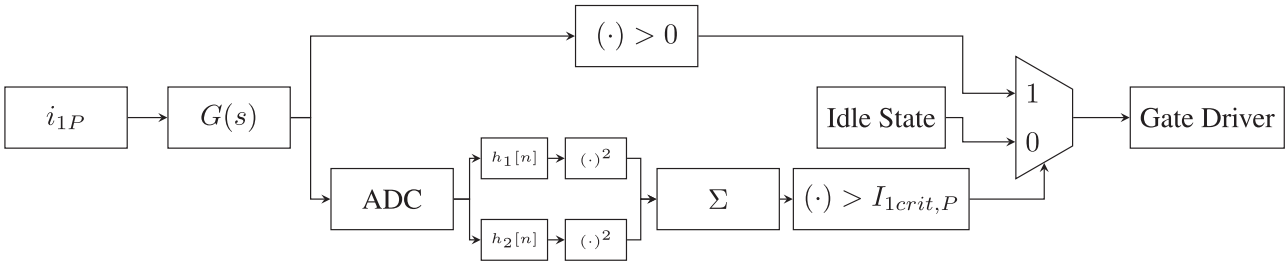

FIGURE 5. Detection and synchronization flow chart, showing how the current i_{1P} defines the switching action. The upper path implements the design discussed in Section III-A, where the zero-crossings of the filtered current signal define the switching moments of the primary inverter. The lower path implements the design discussed in Section IV, which measures the magnitude of the current to determine if the primary should switch. The time delay is dominated by the envelope detector; the anti-resonance filter responds within a few switching periods and the zero-crossing detector is near-instantaneous.

III. PRACTICAL CONSIDERATIONS AND STABILITY

The approach presented up to this point is relatively simple, but any practical system designed only according to Section II will be unstable. Control of the primary inverter by detecting only the zero crossings of i_{1P} introduces instability to the LCCL system. Qualitatively, synchronous inversion tends to inject power at whatever frequency it can be absorbed, which may be dominated by either f_f or a natural response frequency of the primary network. For the system to behave as expected, considerations must be made to ensure power is only injected at f_f. Two filters, pictured in Fig. 5, affect the phase of the zero crossing detection (Section III-A) and implement the envelope detection filter (Section IV).

A. ANTI-RESONANCE FILTER

Resonance, where a positive feedback loop causes the inverter to inject power at a frequency not equal to f_f, will naturally occur in the basic system. Any component of $v_{B,P}$ at a natural response frequency of the primary network, calculated below and given as f_z, will increase the in-phase component of i_{1P}. As the current at f_z increases, zero crossings of i_{1P} become dominated by that frequency, and the spectrum of $v_{B,P}$ becomes dominated by f_z. This positive feedback means that the approach in Section II-B will quickly become unstable unless another measure is taken. Besides significant parasitic losses, no power will be received by the secondary, as the primary and secondary bridges would switch at different frequencies. We introduce a filter that enforces a phase difference between i_{1P} and $v_{B,P}$ at some frequencies to avoid positive feedback. This section derives the design of that anti-resonance filter.

The presence of four reactive components in the primary circuit guarantees that the impedance defined by:

$$Z_{B,P}(j2\pi f) = \frac{\hat{v}_{B,P}}{\hat{i}_{1P}} \tag{8}$$

has four poles and four zeros, with the finite, positive poles and zeros visualized in Fig. 6. One pole is clearly 85 kHz, where i_{1P} and $v_{B,P}$ are decoupled. The other poles are observed by inspection to be 0 and $\pm\infty$. There are also four frequencies where the impedance is zero, $\pm f_{z1}$ and $\pm f_{z2}$.

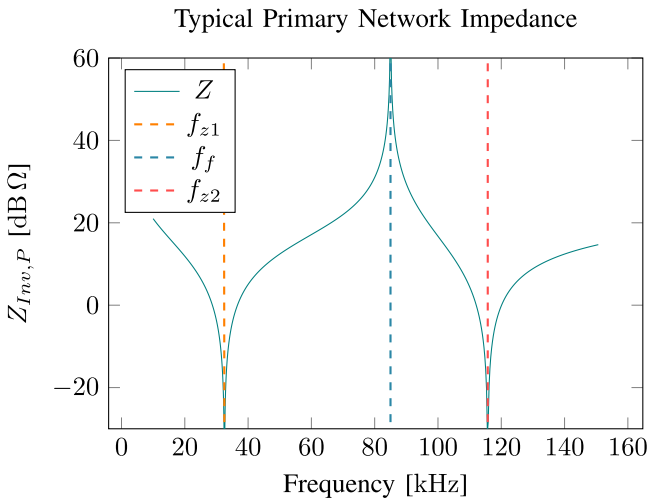

FIGURE 6. Impedance of primary network $Z_{B,P}$. Note that relevant pole and zero frequencies are shown. There are two zeros at the corresponding negative frequencies. There is also a pole at the negative corresponding frequency, at 0, and at ∞.

Although the positive and negative frequencies are algebraic necessities, we only consider positive frequencies.

To simplify the calculation of f_{z1} and f_{z2}, consider the resonant frequencies of each loop of the primary circuit and the coil branch:

$$\begin{aligned} f_{l1} &= \frac{1}{2\pi\sqrt{L_{S,P}C_{P,P}}} \\ f_{l2} &= \frac{1}{2\pi\sqrt{L_{Coil,P}\frac{C_{P,P}C_{S,P}}{C_{P,P}+C_{S,P}}}} \\ f_{coil} &= \frac{1}{2\pi\sqrt{L_{Coil,P}C_{C,P}}} \end{aligned} \tag{9}$$

Given the frequencies defined in (9), the zero frequencies, at which the primary circuit will resonate, are calculated as:

$$f_{z1} = \sqrt{\frac{f_{l1}^2 + f_{l2}^2}{2}}\sqrt{1+\sqrt{1-\frac{4f_{l1}^2 f_{coil}^2}{\left(f_{l1}^2+f_{l2}^2\right)^2}}}$$

$$f_{z2} = \sqrt{\frac{f_{l1}^2 + f_{l2}^2}{2}} \sqrt{1 - \sqrt{1 - \frac{4 f_{l1}^2 f_{coil}^2}{\left(f_{l1}^2 + f_{l2}^2\right)^2}}} \tag{10}$$

In a well-tuned system, where $f_{l1} = f_{l2} = f_f$, we simplify (10) as:

$$f_{z1} = f_f \sqrt{1 - \sqrt{1 - \frac{f_{coil}^2}{f_f^2}}}$$

$$f_{z2} = f_f \sqrt{1 + \sqrt{1 - \frac{f_{coil}^2}{f_f^2}}} \tag{11}$$

A frequency spectrum can be introduced by noise, harmonics, or the natural response to energizing the primary. An anti-resonance filter ensures that $v_{B,P}$ only injects power at f_f, and draws power at f_{z1} and f_{z2}, guaranteeing that i_{1P} will not become dominated by a component at f_{z1} or f_{z2}. The small-signal, linearized relationship between the spectra of i_{1P} and $v_{B,P}$ is addressed more thoroughly in Appendix A. However, here it suffices to note that there is no safe attenuation, below which current at f_{z1} or f_{z2} will not cause resonance. This section defines an anti-resonance filter that avoids the positive feedback phenomenon at the resonant frequencies of the primary circuit.

1) KEY OPERATING PRINCIPLE

To avoid that instability, a first approach is to pass i_{1P} through an anti-resonance filter with the transfer function $G(s)$ and switch inverter states on the zero crossings of $G(i_{1P})$, rather than i_{1P}. The filter needs to be transparent at f_f, so the phase and frequency of $v_{B,P}$ match those of i_{1P}. However, the filter needs to alter the phase of the input signal at f_{z1} and f_{z2}; in all cases, the magnitude is unimportant. The conditions are expressed mathematically as.

$$|\angle G(j2\pi f_{z1})| > 90^\circ \tag{12a}$$

$$|\angle G(j2\pi f_{z2})| > 90^\circ \tag{12b}$$

$$\left|\angle G(j2\pi f_f)\right| = 0 \tag{12c}$$

The conditions in (12a) and (12b) ensure that the applied voltage will draw power from the network, reducing the current at f_{z1} and f_{z2} and preventing positive feedback. Any small noise at either resonant frequency will be reduced as the primary draws power at that frequency. Further, (12c) ensures the primary inverter will inject energy into the network at f_f at near-unity power factor. This is seen in Fig. 7, which illustrates sample phase angles and demonstrates the positive power factor at f_f and negative power factor at the resonant frequencies.

We note that no second-order filter can realize the phase shift requirements expressed in (12a) and (12b). Earlier work gives an active filter solution [11] or a fully passive solution [12], both comprised of two cascaded second-order

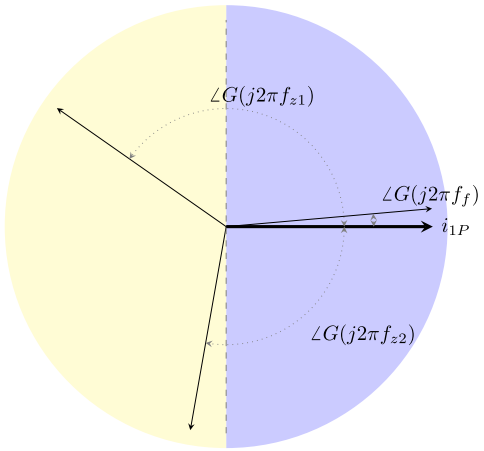

FIGURE 7. Sample phase diagram of the filter at f_{z1}, f_{z2} and f_f; the values shown here are not derived from any circuit but are merely illustrative. The current phase is assumed to be zero. The phase of the voltage is determined by the filter transfer function $G(s)$. On the right half, $|\angle G(s)| < 90^\circ$ and the power factor is positive; meaning the inverter injects power. On the left half, $|\angle G(s)| > 90^\circ$, the power factor is negative, and the inverter draws power.

filters. However, both [11], [12] require inductors in the filters; to avoid the drawbacks of inductors, that filter can be redesigned as a three-ring-filter as described in [37].

The basic approach is to cascade two second-order filters, to achieve the phase required at f_{z1} and f_{z2}. Both filters have the same transfer function:[1]

$$G_{\frac{1}{2}}(s) = \frac{\frac{s}{\omega_f Q}}{1 + \frac{s}{\omega_f Q} + \frac{s^2}{\omega_f^2}}, \tag{13}$$

and both are individually capable of achieving half the required phase shifts: $\pm 45^\circ$ at f_{z1} and f_{z2}, while maintaining near-zero phase shift at f_f. To achieve those phase shifts, the minimum quality factor for each stage is given by

$$Q > \frac{f_f f_{z1}}{f_f^2 - f_{z1}^2} \tag{14a}$$

$$Q > \frac{f_f f_{z2}}{f_{z2}^2 - f_f^2}. \tag{14b}$$

It can be shown that (14b) guarantees (14a) when $L_{Coil,P} > L_{S,P}$. With the assumption of a well-tuned system and noting the redundancy of (14a), the conditions in (14) reduce to

$$Q > \sqrt{\frac{L_{Coil,P}}{L_{1P}} + \sqrt{\frac{L_{Coil,P}}{L_{1P}}}} \tag{15}$$

B. STABILITY ANALYSIS

In Section III-A, an anti-resonance filter was introduced to ensure that the primary inverter draws power at f_{z1} and f_{z2},

[1] Note that the zero-crossing detection is independent of signal magnitude; $G_{\frac{1}{2}}(s)$ can be arbitrarily scaled without affecting operation. For simplicity, we assume a form with unity gain at f_f.

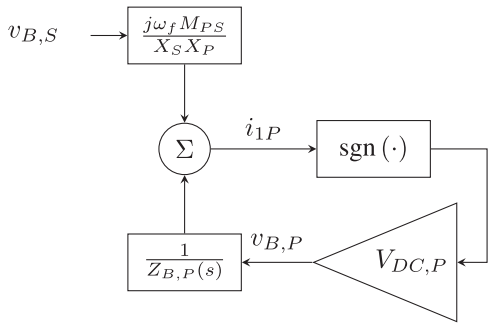

FIGURE 8. Block diagram of the zero-crossing detection sgn(·) in the feedback path with no anti-resonance filtering. The contribution of the secondary voltage excitation $v_{B,S}$ to i_{1P} is determined by (3a), and the effect of the primary voltage $v_{B,P}$ is mediated through $Z_{B,P}$. Note that $v_{B,S}$ is assumed to be monoharmonic at f_f.

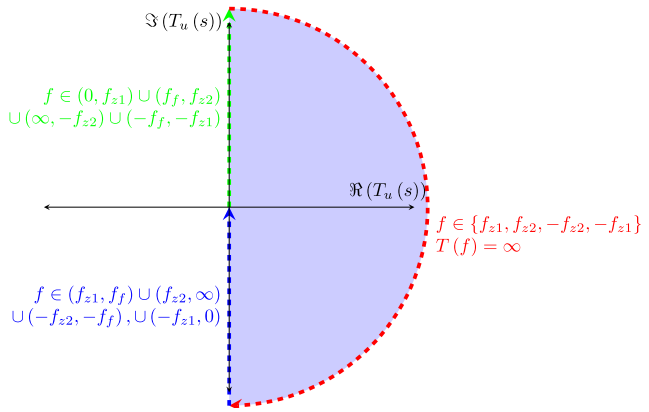

FIGURE 9. Nyquist plot of uncompensated loop gain seen in Fig. 8. Note that since the loop in Fig. 8 shows positive feedback, instability is measured by encirclements about $1 + j0$. The entire shaded region is encircled four times, with two poles with positive frequency and two poles with negative frequency. The outer circumference is at infinity.

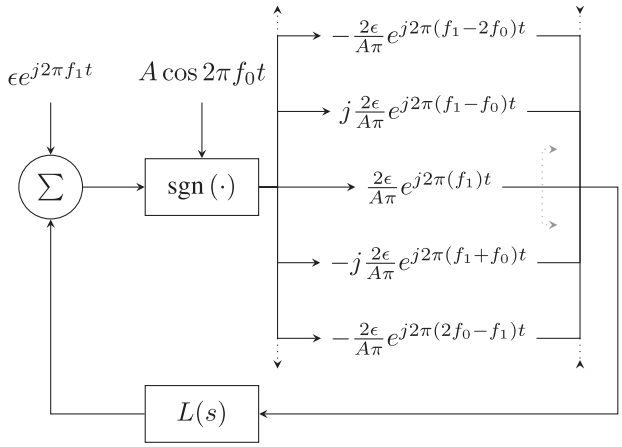

FIGURE 10. Quasi-linear small signal model of the zero-crossing detector. Note the system is not linear: A perturbation at one frequency spreads to other frequencies, and the sidelobes are oddly symmetric about the carrier frequency. The loop gain is measured looking into the gray dashed line. Here, $L(s)$ represents the whole linear portion of the system; in the application discussed here, $L(s)$ includes the admittance $1/Z$ and the anti-resonance filter $G(s)$. For simplicity, only the dominant sidelobes are illustrated here.

rather than injecting power. This section addresses the effect of those measures quantitatively. In Section III-B1, the instability of the system without the anti-resonance filter is quickly proved through local linearization. Section III-B2 derives the necessary conditions for system stability using a quasi-linearized model, which can be expressed as a modification of the linear portion of the loop gain. That section also discusses the characteristics of unstable system behavior. Section III-C summarized the stability criteria.

1) PROOF OF INSTABILITY WITHOUT ANTI-RESONANCE FILTER

In Section III-A, an anti-resonance filter is developed to avoid positive feedback resonance. A more rigorous stability analysis is presented here, assuming a portion of i_{1P} is induced by the secondary; this section evaluates stability in the presence of a current-inducing secondary. A block diagram of the system with zero-crossing detection is shown in Fig. 8.

A fully-linear approximation of the zero-crossing detector is calculated in Appendix A, the result being that a small-signal, linear approximation of sgn(·) is a scalar gain of $2/(A\pi)$, where A is the magnitude of the carrier current at the dominant frequency; here, the portion of i_{1P} at f_f induced on the primary by the secondary. The linear system can demonstrate instability but may not guarantee stability. The major contribution of the secondary is in setting the steady-state amplitude A of the carrier component of i_{1P}. This gives a linearized open-loop gain of

$$\frac{2}{A\pi} \tag{16}$$

The instability of this system can be readily proved with a Nyquist plot. Note that the feedback is positive, so the encirclements should be counted about the critical point $1 + j0$, rather than $-1 + j0$. By inverting the impedance in Fig. 6, it can be observed that the open-loop transfer function has poles at f_{z1} and f_{z2}, and zeros at 0 and ∞. The phase at every frequency is $\pm 90^\circ$ because there are only reactive elements in the circuit. The Nyquist plot of the uncompensated open-loop gain $T_u(s)$ is given in Fig. 9.

Both positive and negative frequencies are considered in Fig. 9. As expected, the loop gain pole frequencies f_{z1} and f_{z2} cause four encirclements, and place poles of the closed-loop system in the right-hand plane. Without the anti-resonance filter, the system is unstable.

2) STABILITY CONDITIONS WITH ANTI-RESONANCE FILTER

The inclusion of the anti-resonance filter $G(s)$ visualized in Fig. 11 can stabilize the system. Because the zero-crossing detector introduces additional frequencies, all relevant frequencies should be considered in any closed-loop analysis.

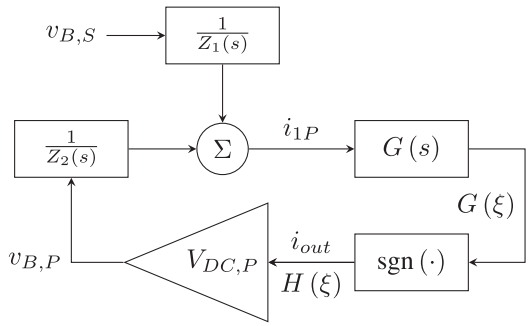

FIGURE 11. Block diagram of the zero-crossing detection sgn(·) in the feedback path with no anti-resonance filtering. The contribution of the secondary voltage excitation $v_{B,S}$ to i_{1P} is mediated through the impedance Z_1, and the effect of the primary voltage $v_{B,P}$ is mediated through Z_2. The spectra of the input and output to the zero-crossing detector are shown as $G(\xi)$ and $H(\xi)$, respectively.

The flaw with the fully-linearized model given in Appendix A is that it assumes an infeasible output of the zero-crossing detector, so any analysis done using only the fully linear model is inaccurate. Counterexamples exist where the fully linearized model predicts stability, but a simulation demonstrates instability. In this section, the system is modeled with the full quasi-linearized model derived in Appendix A, where the "transfer function" of the zero-crossing detector is given by

$$H_n(\xi) = \sum_{k=-\infty}^{\infty} \left(\frac{2(-j)^k}{A\pi} G_n(\xi - kf_0) \right). \tag{17}$$

After the model is developed, a method to test for stability numerically is discussed, along with an approximate analytical method.

Here, the zero-crossing detector acts in the presence of the carrier signal (noted as $A\cos(2\pi f_0 t)$ in Fig. 10) and in a loop with a linear component $L(s)$. For our purposes, $L(s) = G(s)/Z_{B,P}(s)$. Assume that noise is injected before the current sensor, but the open-loop gain is measured after, visualized in Fig. 10 with the noise $\epsilon d^{j2\pi f_1 t}$ and the loop gain measured from the gray dashed line, where ϵ is an infinitesimally small scalar value.

We consider the spectrum of the noise signal as it passes through the loop. Let $i_0(\xi)$ be the small-signal spectrum of the noise signal at a frequency f, modeled as a Dirac function in the frequency domain:

$$i_0(\xi) = \epsilon\delta(\xi - f_1). \tag{18}$$

The small-signal zero-crossing detector output spectrum $v_0(\xi)$ is given by

$$v_0(\xi) = \epsilon \sum_{k=-\infty}^{\infty} \left(\frac{2(-j)^k}{A\pi} \delta(\xi - f_1 - kf_0) \right) \tag{19}$$

In a feedback loop with a linear transfer function $L(s)$, the spectrum of the feedback input to the zero-crossing detector i_1 is given by

$$i_1(\xi) = \epsilon \sum_{k=-\infty}^{\infty} \left(\frac{2(-j)^k}{A\pi} \delta(\xi - f_1 - kf_0) L(j2\pi\xi) \right) \tag{20}$$

The linear function $L(s)$ discussed here is includes the anti-resonance filter $G(s)$ and the admittance $1/Z(s)$.

The output of the zero-crossing detector is given by

$$v_1(\xi) = \epsilon \sum_{l=-\infty}^{\infty} \left(\frac{2(-j)^l}{A\pi} \sum_{k=-\infty}^{\infty} \left(\frac{2(-j)^k}{A\pi} \delta L(\xi, k, l) \right) \right)$$

$$\delta L(\xi, k, l) = \delta(\xi - f_1 - kf_0 - lf_0) L(j2\pi\xi - lf_0); \tag{21}$$

comparing $v_1(f_1)$ and $v_0(f_1)$ gives

$$v_1(f_1) = v_0(f_1) \frac{2}{A\pi} \sum_{k=-\infty}^{\infty} L(j2\pi f_1 + kf_0), \tag{22}$$

which suggests the open-loop transfer function has the periodic form

$$T(s) = \frac{2}{A\pi} \sum_{k\in\mathbb{Z}} L(s + j2\pi k f_0) \tag{23}$$

Note that the loop gain is inversely proportional to the amplitude of the carrier signal.

A precise, analytical stability test for an infinite-series transfer function is beyond the scope of this work. Here, stability tests are derived using a Nyquist plot,[2] which can be generated with a truncated series.[3] Because the loop has positive feedback, encirclements are counted about the point $(1 + j0)$.

With no parasitic resistance in the primary, two classes of encirclements are considered. First, those with infinite radius, where scaling the loop gain has no effect, and second, those with finite radius, where the loop gain can be scaled to stabilize the system.

3) ENCIRCLEMENTS WITH INFINITE RADIUS

Because the loop gain $T(s)$ is periodic, the number of poles in one period of $T(s)$ is equal to the number of poles in $L(s)$. Further, the behavior of $T(s)$ near any pole is dominated by the corresponding pole in $L(s)$. Mathematically,

$$L(s - j2\pi f_0) \to \infty \Rightarrow$$

$$T(s) \approx \frac{2}{A\pi} L(s - j2\pi k f_0) = \frac{2}{A\pi} L(j2\pi(\xi - f_0)), \tag{24}$$

where k is any integer. So, it is sufficient to consider potential encirclements with infinite radius on the linear system $L(s)$. The essential function of the anti-resonance filter is to modify the phase of the Nyquist plot in Fig. 9. The phase of the anti-resonance filter $G(s)$ varies on the range $(-180°, 180°)$.

[2]In this discussion, assume that there is no parasitic resistance in the system, so some portions of the Nyquist plot will have infinite radius.

[3]Because there are zeros at $\pm\infty$ in $L(s)$, the system can be truncated with reasonable accuracy by neglecting frequencies $|\xi| \gg |f_{z2}|$.

TABLE 2. Phase Response of Compensated Loop

Frequency Range	Phase Range
$(0, f_{z1})$	$(270°, 90° + \angle G(j2\pi f_{z1}))$
f_{z1}	$(90° + \angle G(j2\pi f_{z1}), -90° + \angle G(j2\pi f_{z1}))$
(f_{z1}, f_f)	$(-90° + \angle G(j2\pi f_{z1}), -90°)$
(f_f, f_{z2})	$(90°, 90° + \angle G(j2\pi f_{z2}))$
f_{z2}	$(90° + \angle G(j2\pi f_{z2}), -90° + \angle G(j2\pi f_{z2}))$
(f_{z2}, ∞)	$(-90° + \angle G(j2\pi f_{z2}), -270°)$

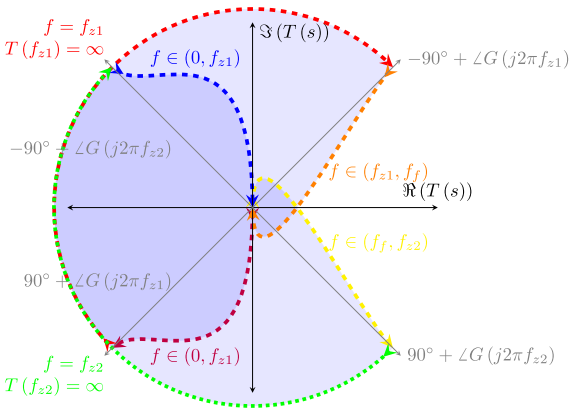

FIGURE 12. Nyquist plot of the linear, compensated loop gain $L(s)$ seen in Fig. 11. Note that since the feedback is positive, instabilities are found by encirclements of the point $1 + j0$. Only positive frequencies are shown here, but the pertinent features of the Nyquist plot for negative frequencies are similar and easily extrapolated. Poles of $L(s)$ correspond exactly to poles of $T(s)$.

The angle ranges of the compensated loop gain, including the zero-crossing detector, anti-resonance filter, DC voltage gain, and impedance in Fig. 11 are given in Table 2.

To ensure the pole frequencies f_{z1} and f_{z2} do not encircle the critical point, the phase of $G(s)$ at f_{z1} and f_{z2} is restricted such that

$$-90° + \angle G(j2\pi f_{z1}) > 0 \tag{25a}$$

$$90° + \angle G(j2\pi f_{z2}) < 0 \tag{25b}$$

Note that the conditions in (25a) and (25b) are equivalent to (12a) and (12b), respectively; the inclusion of the anti-resonance filter as designed is sufficient to avoid encirclements of the critical point with infinite radius. This means that, once the anti-resonance filter is included, any encirclements can be avoided by sufficiently reducing the loop gain when the anti-resonance filter is included.

4) ENCIRCLEMENTS WITH FINITE GAIN

The conditions in (25) ensure that there will not be an encirclement with infinite radius, but, as seen in Fig. 12, there can be an encirclement with finite radius. A sufficiently dominant carrier current reduces the small-signal loop gain; this section defines the minimum carrier current (induced by the secondary) to ensure there are no encirclements in the Nyquist plot and guarantee stability. In this section, a practical test is defined. Then, to gain more insight, an approximation of a sufficient condition is developed.

The most comprehensive test for stability is with a Nyquist plot of the quasi-linear loop, with the loop $T(s)$ defined in (23). Note that (23) implies that the open-loop transfer function is always periodic on f_0. Because

$$\lim_{s\to\infty} \frac{G(s)}{Z(s)} \to 0, \tag{26}$$

there must be a reasonable approximation of $T(s)$ by a finite series. A Nyquist-like plot can be constructed with that finite series on the interval $\xi \in [-f_f/2, f_f/2]$, and the plot is measured for encirclements.

Setting the turn-on threshold forces $A > I_{1crit,P}$, with no feedback and no instability when $I_{1P} < I_{1crit,P}$. The threshold $I_{1crit,P}$ can be defined to force A to be sufficiently great that none of the x-axis crossings encircle the critical point $(1 + j0)$. That is, $I_{1crit,P} > A_{min}$, where A_{min} is the minimum carrier amplitude to move the real-axis crossings to the interval [0, 1], removing any encirclements.

Given the graphical method to determine stability, it is desired to define a more informative and intuitive stability criterion. Because $T(s)$ is periodic, it is sufficient to consider potential encirclements on the range $\xi \in [0, f_f]$. On that range, consider the positive x-axis crossing of the Nyquist plot.

Let f_{e1} be a frequency where the phase of the anti-resonance filter is 90°, and f_{e2} is the frequency where the phase of the anti-resonance filter is −90°. With a high-Q-factor anti-resonance filter, f_{e1} and f_{e2} will be near f_f, with $f_{e1} < f_f$ and $f_{e2} > f_f$. The linear gain $L(s)$ is $G(s)/Z_{B,P}(s)$, and the angles $\angle Z_{B,P}(j2\pi f_{e1}) = 90°$ and $\angle Z_{B,P}(j2\pi f_{e2}) = -90°$. Thus, $L(j2\pi f_{e1})$ and $L(j2\pi f_{e2})$ are real. Further, with a high-Q-factor anti-resonance filter,

$$f_{e1} + f_{e2} \approx 2f_f. \tag{27}$$

Because of the additional frequencies introduced by the zero-crossing detector, the Nyquist plot should be generated with $T(s)$, rather than $L(s)$. Because of the zeros at high frequencies and 0, and because f_{e1} is close to f_f, most terms of (23) can be neglected:

$$T(j2\pi f_{e1}) \approx \frac{2}{A\pi}\left(L\left(j2\pi\left(f_{e1} - 2f_f\right)\right) + L(j2\pi f_{e1})\right). \tag{28}$$

Substituting (27) into (28) yields

$$T(j2\pi f_{e1}) \approx \frac{2}{A\pi}\left(L(-j2\pi f_{e2}) + L(j2\pi f_{e1})\right) \tag{29}$$

Because the system is real, $L(-s) = L(s)^*$. Further, because $L(-j2\pi f_{e2})$ is real,

$$T(j2\pi f_{e1}) \approx \frac{2}{A\pi}\left(L(j2\pi f_{e2}) + L(j2\pi f_{e1})\right). \tag{30}$$

By a similar argument,

$$T(j2\pi f_{e1}) \approx T(j2\pi f_{e2}), \tag{31}$$

so the stability condition refers to the system behavior at both frequencies.

The stability condition is the real axis crossings of $T(j2\pi\xi)$, occurring approximately at f_{e1} and f_{e2}, are less than one. This is expressed as

$$\frac{2}{A\pi}\left(\frac{G(j2\pi f_{e1})}{Z_{B,P}(j2\pi f_{e1})} + \frac{G(j2\pi f_{e2})}{Z_{B,P}(j2\pi f_{e2})}\right) < 1 \tag{32}$$

This can be further simplified by noting that $G(s)$ is comprised of two second-order filters defined in (13). The anti-resonance filter gain at f_{e1} and f_{e2} is $\pm j/2$; the condition in (32) can be simplified and solved for A:

$$\frac{1}{\pi}\left(\frac{j}{Z_{B,P}(j2\pi f_{e1})} + \frac{-j}{Z_{B,P}(j2\pi f_{e2})}\right) < A \tag{33}$$

Note that the phase of $Z_{B,P}(j2\pi f_{e1})$ is 90°, and the phase of $Z_{B,P}(j2\pi f_{e2})$ is −90°, so both summands are real and positive. The system will be stable when the carrier current (induced by the secondary at f_f) is greater than the threshold in (33). This can be guaranteed by detecting the carrier current envelope, and only initiating primary switching when I_{1P} satisfies the condition on A in (33).

C. STABILITY CONDITIONS SUMMARY

This section summarizes the conditions for system stability developed in Section III-B. To avoid instability, the anti-resonance filter should provide the phase characteristics in (12), which is assumed to be implemented as two cascaded second-order analog filters. Further, the turn-on threshold current $I_{1crit,P}$ should be high enough to avoid turn-on by a neighboring pad, addressed in (7), and should be high enough to avoid local instability, addressed in (33). These three conditions guarantee that during power transfer, the system is stable.

It may also be informative to consider stability in the time domain, rather than the frequency domain. Such an approach is treated in Appendix B, which also evaluates the stability of the system discussed in Sections V and VI.

1) NOTE ON INTERFERENCE FROM THE SECONDARY

The value of Z defined here typically considers only the primary network, not any effects from the secondary. The extra element theorem (EET) can be used to modify the expression in (33) to include the effects of the secondary [38]. The EET provides a scaling factor that relates the impedance with the extra element (in this case, impedance reflected from the secondary network to the primary network) to the impedance without it. The scaling factor γ for the expression in (33), which is inversely proportional to the impedance, is given by

$$\gamma = \frac{1 - \frac{s^2M_{PS}^2}{Z_{secondary}Z_d}}{1 - \frac{s^2M_{PS}^2}{Z_{secondary}Z_n}}, \tag{34}$$

where Z_n and Z_d are nulling and direct impedances and $Z_{secondary}$ is the impedance looking into the secondary from the coil, i.e.,

$$Z_{secondary} = sL_{Coil,S} + \frac{1}{sC_{S,S}} + \frac{sL_{S,S}}{1 + s^2L_{S,S}C_{P,S}} \tag{35a}$$

$$Z_n = sL_{Coil,P} + \frac{1}{sC_{S,P}} + \frac{sL_{S,P}}{1 + s^2L_{S,P}C_{P,P}} \tag{35b}$$

$$Z_d = sL_{Coil,P} + \frac{1}{sC_{S,P}} + \frac{1}{sC_{P,P}} \tag{35c}$$

Typically, at the f_{e1} and f_{e2}, the correction factor γ will be small, on the order of a few decibels. The effect should be considered but is not the main driving force of instability.

2) NOTE ON BOUNDED INSTABILITY

Instability, as described here, represents any deviation away from the steady-state condition. Instability may not lead to system failure but may simply allow other frequencies to be introduced into $v_{B,P}$, which leads to some power oscillation. If the conditions described here are too exacting, some instability and power ringing may be allowed; especially if a strong EMI filter is included on the primary and secondary. For a conceptual argument for why instability is bounded, note that only the first-order effects have been discussed here. However, the gain decreases as the noise signal increases from an infinitesimal magnitude, bounding the gain and eventually placing the real-axis crossings of the Nyquist plot with a finite radius exactly at the critical point.

Instability presents as an increasing component of $v_{B,P}$ and i_{1P} at some frequency. However, as the component of i_{1P} at that frequency increases, that component becomes the carrier signal, and A begins to increase, which eventually causes (33) to be satisfied. The bounded nature of the instability can also be understood by noting that, when second-order effects are considered, the loop gain is decreased for non-infinitesimal ϵ. As the noise signal increases, the loop gain decreases, and eventually the system becomes stable. A more thorough analysis is beyond the scope of this work, but can easily be verified in simulation by allowing the condition in (33) to be violated by a small margin. For reference, a screen capture of a hardware result of a system with bounded instability is shown in Fig. 13. In that figure, note the power ripple just after turn on and just before turn off.

IV. ENVELOPE DETECTION

So far in this work, references have been made to the turn-on condition

$$I_{1P} < I_{1crit,P}, \tag{36}$$

but no mention of how the envelope of I_{1P} can be measured, especially when i_{1P} contains multiple frequencies. The turn-on condition should be measured only on the component of i_{1P} at f_f and should give a constant output, regardless of the phase of the input signal. This section describes a discrete-time

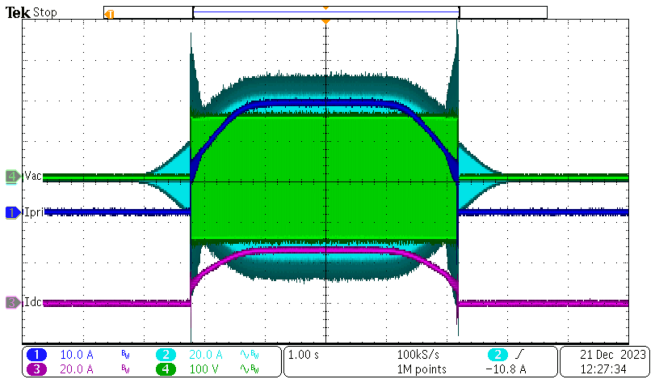

FIGURE 13. Oscilloscope screen capture from a hardware test. Primary switching is initiated before $I_{1P} > I_{1crit,P}$. Note the widening of the "Ipri" line, which represents the DC bus current I_{pri}, just after the turn-on and just before the turn-off. The introduction of current at f_{e1} and f_{e2} causes beat interference, introducing ripple into the DC. That beat interference is also shown in the current i_{1P}, shown in light blue but whose label is hidden in the screen capture. It can be seen that in that unstable region, the peak current increases. As the interference from the current at f_{e1} and f_{e2} is reduced, the constructive interference decreases, and the current i_{1P} approaches normalcy.

envelope detection filter, which can also attenuate other frequencies. The basic approach is highlighted in Section IV-A, with Section IV-B describing key frequency response characteristics of the filter, and Sections IV-B and IV-C discussing how the filter should be designed. Section IV-E summarizes the envelope detector design requirements.

A. APPROACH OVERVIEW

To achieve phase independence, the envelope detection filter is comprised of two discrete, orthogonal filters with complementary phases and equal magnitude gain at f_f; let the filters be defined as $h_1[n]$ and $h_2[n]$ and let the samples of i_{1P} be given as $x[n]$, and let the output of the envelope detector be given by $y[n]$. Then

$$y[n] = \sqrt{\left(\sum_k h_1[k]x[n-k]\right)^2 + \left(\sum_k h_2[k]x[n-k]\right)^2} \tag{37}$$

Suppose i_{1P} is monoharmonic with magnitude α and h_1 and h_2 have unity magnitude gain and complementary phase, such that

$$x[n] = \alpha\cos(2\pi f + \phi_1) \tag{38a}$$

$$\sum_n h_1[n]x[k-n] = \alpha\cos(\phi_1 + \phi_2) \tag{38b}$$

$$\sum_n h_2[n]x[k-n] = \alpha\cos\left(\phi_1 + \left(\phi_2 + 90^\circ\right)\right) \tag{38c}$$

for some angles ϕ_1 and ϕ_2. Substituting (38b) and (38c) into (37) yields

$$y[k] = |\alpha|, \tag{39}$$

which demonstrates the desired phase-independence properties. A simple approach is let $h_1[n]$ and $h_2[n]$ be derived from a basic low-pass filter $w[n]$, as

$$h_1[n] = 2w[n]\cos(2\pi F_{conv}n) \tag{40a}$$

$$h_2[n] = 2w[n]\sin(2\pi F_{conv}n), \tag{40b}$$

where F_{conv} is a discrete-time frequency, and the necessary properties of $w[n]$ are addressed in Sections IV-B and IV-C. If $F_{conv} = 0.25$, then half the terms in both $h_1[n]$ and $h_2[n]$ are eliminated, simplifying the filters. In that case, both filters will have the strongest response when f_f aliases to $F_{conv} = 0.25$, which requires the sampling frequency f_{sam} to be selected:

$$f_{sam} = \frac{4}{k}f_f, \quad k = 1, 3, 5, \ldots \tag{41}$$

With the filter structure defined, consideration is now given characteristics and implementation of the low-pass filter.

B. SELF-INDUCED CURRENT ATTENUATION

The primary may continue switching even after the secondary is removed; to avoid that, the low-pass filter should attenuate the current induced only by the primary. This section defines at what frequencies such a phenomenon may occur and defines a necessary characteristic of the low-pass filter.

Consider the case where some current $\bar{I}_{ind}$ is induced in $\bar{I}_{1P}$; some component of the current is induced from the secondary and some component is induced by $\bar{V}_{B,P}$. Without loss of generality, let the angle $\angle\bar{I}_{1P} = 0$. Let $Z_{B,P}$ again be the impedance seen by the primary inverter. Note that with no resistive elements, $\angle Z_{B,P} = \pm 90^\circ$. Then, we observe the relationship:

$$\bar{I}_{1P} = \bar{I}_{ind} + \frac{|\bar{V}_{B,P}|\angle G(s)}{Z_{B,P}} \tag{42}$$

If there is no induced current, (42) only has a solution when $\angle G(s) = \angle Z_{B,P}$. For convenience, let us define the following quantities:

$$\theta_{Zf} = \angle Z_{B,P}(j2\pi f) \tag{43a}$$

$$\theta_{Gf} = \angle G(j2\pi f) \tag{43b}$$

Both quantities describe how much the voltage leads the current at the primary inverter, although both refer to different portions of the current i_{1P}.

When the secondary does not induce any component of the current $\bar{I}_{1P}$ and $\theta_{Zf} \neq \theta_{Gf}$, the frequency is unstable and there is no solution to (42). That instability is observed by letting the current $A \to 0$ in the stability criterion (33). Consider a moment where $\theta_{Zf} > \theta_{Gf}$. At that moment, the current forced by the inverter leads the total current, and the phase of the total current increases. The rate of change is beyond the scope of this paper, suffice it to note that the phases of the voltage and current are unstable and increasing. A continuously increasing phase is equivalent to a higher frequency; thus, when $\theta_{Zf} > \theta_{Gf}$, the frequency will increase.

Similarly, when $\theta_{Zf} < \theta_{Gf}$, the frequency decreases. We refer to the equilibrium frequencies f_{e1} and f_{e2} defined previously where $\theta_{Zf} = \theta_{Gf}$, and define them in terms of the anti-resonance filter quality factor Q:

$$f_{e1} = \frac{f_f}{2Q}\left(\sqrt{1+4Q^2} - 1\right) \tag{44a}$$

$$f_{e2} = \frac{f_f}{2Q}\left(\sqrt{1+4Q^2} + 1\right). \tag{44b}$$

With f_{e1} and f_{e2} defined and the frequency drift phenomena as described at those frequencies, the equilibrium frequencies are stable when the condition:

$$\lim_{f \to f_e} \frac{\left(\theta_{Zf} - \theta_{Gf}\right)}{(f - f_e)} < 0 \tag{45}$$

is met; otherwise, they are unstable.

Note that the frequencies defined in (44) depend on Q. To preserve the integrity of the signal at f_f, Q should generally be as high as possible to minimize the contribution of $v_{B,P}$ to i_{1P} at f_{e1} or f_{e2}. Further note that as $Q \to \infty$, $f_{e1}, f_{e2} \to f_f$ and $Z_{B,P}(f_f) \to \infty$. Thus, a sufficiently high Q will ensure that during steady state operation, the current at f_f dominates the current at either equilibrium frequency.

The steady-state current is determined by the magnitudes $|Z_{B,P}(j2\pi f_{e1})|$ and $|Z_{B,P}(j2\pi f_{e2})|$. When the secondary no longer induces a current i_{1P} at f_f, the primary inverter will drift to operate at f_{e1} or f_{e2}, given in (44). At either of those operating points, the primary network may consume a large amount of reactive power, and the current i_{1P} may be high, possibly perpetuating the operation of the primary inverter. The envelope filter described in (37) should attenuate any contributions from the current at f_{e1} or f_{e2}. Let f_{e1} and f_{e2}, continuous-time frequencies, alias to F_{e1} and F_{e2}, discrete-time frequencies. Then let the discrete-time frequency bandwidth β be

$$\beta_1 = \min\left(|F_{conv} \pm F_{e1} + n|\right), \quad n \in \mathbb{Z} \tag{46a}$$

$$\beta_2 = \min\left(|F_{conv} \pm F_{e2} + n|\right), \quad n \in \mathbb{Z} \tag{46b}$$

If F_{e1} and F_{e2} are near 0 or 0.25, $\beta_1 \approx \beta_2 \approx 0.25$, which is the maximum possible value.

The first property of the low-pass filter is that the stopband should begin at most by β, with a maximum stopband gain of $W(\beta)$:

$$W\left(\beta_1\right) <= \frac{\pi}{4V_{DC,P}}(2)Z_{B,P}\left(2\pi f_{e1}\right) I_{1crit,P} \tag{47a}$$

$$W\left(\beta_2\right) <= \frac{\pi}{4V_{DC,P}}(2)Z_{B,P}\left(2\pi f_{e2}\right) I_{1crit,P}; \tag{47b}$$

those expressions are inversely proportional to the AC bridge voltage and the gain of the anti-resonance filter at f_{e1}, and proportional to the impedance and the turn-on threshold. This ensures the primary cannot be active without a secondary.

C. DC OFFSET AND PHASE SENSITIVITY

The sensitivity of the discrete-time filter to a DC offset is determined by the sensitivity of the lowpass filter to the frequency $F = 0.25$. The required attenuation depends on the maximum expected DC offset; here, let the maximum desired DC gain of the final filter be W_{DC}. Then the design requirement for the lowpass filter is

$$W(0.25) \leq W_{DC} \tag{48}$$

The DC gain can interfere constructively or destructively with the signal gain, resulting in output variance. Ideally, the DC sensitivity is 0, but that may not be perfectly achievable.

Similarly, any response of the lowpass filter at $F = 0.5$ will also manifest as a phase dependence in the envelope detector. Even if there is no DC offset, any sensitivity will cause a phase dependence on the envelope detector. The attenuation at $F = 0.5$ should be as low as possible while limiting the filter length to a reasonable size.

The passband should be sized to include some robustness to frequency differences; a few hundred hertz is generally sufficient. Some variance in filter passband sensitivity affects the effective turn-on threshold current but does not affect system performance as much as other lowpass filter design parameters.

D. CONTROL SYSTEM TIMING

The response time of the control system is dominated by the realization of the envelope detector. As seen in Fig. 5, three processes contribute to the delay. First, the anti-resonance filter adds some delay but generally responds to a new condition within a few switching periods. Second, the zero-crossing detector is realized with a comparator, and the delay is dominated by the gate drivers themselves — delay in the zero-crossing detector is on the order of tens of nanoseconds.

The envelope detector, however, introduces much more delay. A typical, reasonably-sized filter can have better 10 and 20 taps. Further, the sampling frequency can be below the switching frequency. In Sections VI and V, the sampling frequency is around 30 kHz, leading to a response time of hundreds of microseconds. While the specifics of the timing depend on the sampling frequency and the number of taps in the envelope detector, the envelope detector will be the limiting factor in the control system timing.

E. ENVELOPE DETECTOR SUMMARY

The envelope detector can be implemented by multiplying a lowpass filter $w[n]$ with two orthogonal filters to generate $h_1[n]$ and $h_2[n]$, as in (40). Letting $F_{conv} = 0.25$ simplifies the implementation.

The lowpass filter should be designed to:

- Have a relatively small passband, on the order of a few hundred Hertz. Moderate variation is allowed within the passband.
- Have a gain at β that satisfies (47).
- Have the DC gain sensitivity at $F = 0.25$
- Have as low sensitivity as possible at $F = 0.5$ while keeping the filter length reasonable.

TABLE 3. Simulated Component Values

Component	Value	Component	Value
$V_{DC,P}$	565 V	$V_{DC,S}$	565 V
$L_{S,P}$	5.62 µH + 5 mΩ	$L_{S,S}$	3.35 µH + 5 mΩ
$C_{P,P}$	631 nF	$C_{P,S}$	1.04 µF
$C_{C,P}$	415 nF	$C_{C,S}$	990 nF
$L_{Coil,P}$	14.2 µH + 5 mΩ	$L_{Coil,S}$	8.10 µH + 5 mΩ
max (M_{PS})	1.61 µH	min (M_{PS})	534 pH
max (M_{PP})	−35.3 nH	min (M_{PP})	−73.7 nH
L_{bus}	100 nH	R_{bus}	1 mΩ
C_{bus}	200 µF		

Within these rough design parameters, the design and choice of the lowpass filter are beyond the scope of this work.

V. SIMULATION VALIDATION

The design approach presented thus far aims to apply to any LCCL system; that is, the coils and compensation are defined to satisfy power transfer, EMI, or other requirements, and the proposed synchronous inversion control scheme is wrapped around an existing design. To validate the scheme in terms of detection, synchronization, and stability, the proposed scheme is tailored for an existing hardware system with a primary pad and a secondary pad. The relevant inductances have been simulated in a FEM solver, and the entire system is simulated in a Simulink/Plecs environment. In Section V-A, the basic system parameters are defined. Section V-B assesses the system stability as discussed in Section III-B. Sections V-D to V-F describe the results of various tests.

A. SYSTEM OVERVIEW

The primary coils are a DD design, with the magnetic field orthogonal to the direction of travel. Using the axes defined in the static WPT SAE standard [39], the primary coils measure 2 m in the y-dimension and 1 m in the x-dimension. The secondary coils have a complementary DD geometry, measuring 1 m in the x-dimension by 1 m in the y-dimension. The system values are given Table 3. Note that a small, practical resistance has been included on the inductors for simulation.

The self and mutual inductances are measured at a variety of y-misalignments, replicating the varying coupling as a vehicle passes over several subsequent primary pads. In the simulation, the vehicle passes over the primary pads at 30 km/h. The simulations include representative DC bus inductance, resistance, and capacitance values, which tend to filter out the power ripple at double the switching frequency, seen in Fig. 14; the DC bus is assumed to be identical for both the primary and the secondary and the values are also reported in Table 3. To simplify the graphs and remove the power ripple, the power is passed through a second-order low-pass filter with a corner frequency of 500 Hz; extensive work exists

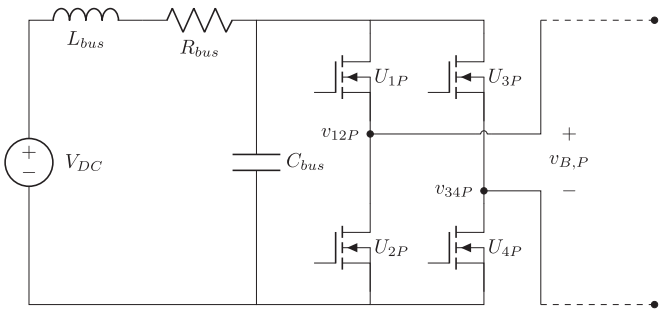

FIGURE 14. Diagram of H-bridge with bus capacitance and parasitic inductance and resistance.

on eliminating the power ripple; that work is not replicated here.

With (11), the resonant frequencies are determined to be

$$f_{z1} = 41.3\,\text{kHz} \tag{49a}$$

$$f_{z2} = 114\,\text{kHz}, \tag{49b}$$

The design discussed to this point is fixed before the control scheme is implemented. The discussion now turns to the requirements to ensure stability.

B. STABILITY ANALYSIS

Given those design requirements, the stability can be analyzed. Given the resonant frequencies defined in (49), the minimum quality factor is determined to be $Q = 1.67$, as per (15). Ensuring the quality factor exceeds 1.67 meets the first of the three conditions discussed in Section III-C. A quality factor of $Q = 5$ is selected for the anti-resonance filter, satisfying that condition and placing the equilibrium frequencies f_{e1} and f_{e2} at

$$f_{e1} = 76.9\,\text{kHz} \tag{50a}$$

$$f_{e2} = 93.9\,\text{kHz}. \tag{50b}$$

The other stability requirements are that the conditions in (7) and (33) are satisfied, requiring the following, respectively:

$$I_{1crit,P} > 1.67\,\text{A} \tag{51a}$$

$$I_{1crit,P} > 33.8\,\text{A} \tag{51b}$$

Although only one primary pad was used in the simulation, M_{PP} was calculated for a reasonably-placed hypothetical second primary pad for (51a). As discussed in Section III-C1, the secondary can reduce the impedance somewhat, and the current threshold $I_{1cirt,P}$ should be somewhat higher. The system parameters described here imply that an additional 1.4 dB on the turn-on threshold should ensure stability; so let

$$I_{1crit,P} = 40\,\text{A} \tag{52}$$

Recall that the condition in (33) is only approximate, and a Nyquist plot is necessary to confirm stability. The Nyquist plot described in Section III-B4 with $A = I_{1crit,P} = 75$ A is shown

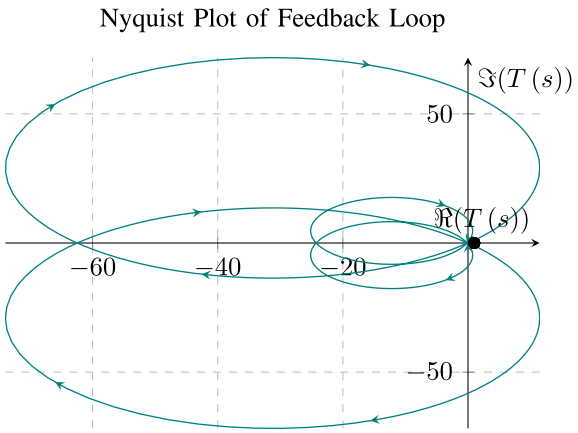

FIGURE 15. Nyquist plot of the loop gain. As discussed in Section III-C1, the loop gain is periodic. From this perspective, it is observed that there are no encirclements with infinite or near-infinite (restricted only by parasitic resistance) radius.

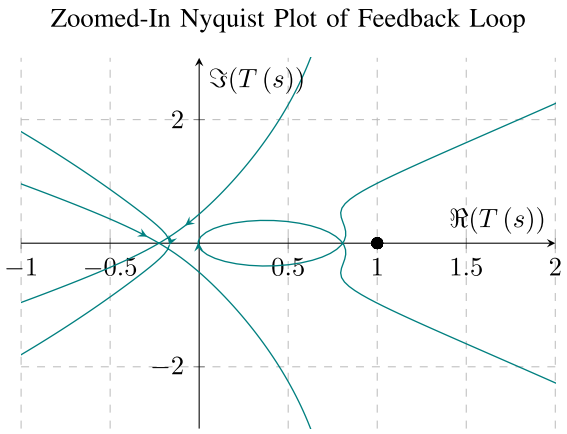

FIGURE 16. Zoomed-in Nyquist plot with $A = I_{1crit,P} = 40$ A. The chosen value of $I_{1crit,P}$ forces the x-axis crossings to occur to the left of unity, guaranteeing there are no encirclements of the critical point and guaranteeing stability.

in Fig. 15, with a zoomed-in version shown in Fig. 16. As the magnitude of the carrier increases, the x-axis crossings will move towards the origin, with no effect on the stability of the system.[4] By assuming a small series resistance, the Nyquist plot differs slightly from that shown in Fig. 12, replacing the infinite radius with a finite radius. However, the four sections with infinite radius in Fig. 12 correspond to the large loops in Fig. 15. In Figs. 15 and 16, the both primary inductors are assumed to have the 5 mΩ resistance shown in Table 3.

Four tests are completed here, described more fully in Sections V-C to V-F, respectively:

- Benchmark pulse test: The primary and secondary continuously operate on a shared clock. This has no synchronization or detection, and the shared clock is unrealizable.
- Standard pulse test: The system runs as described thus far; typical operation.
- Half pulse test: While coupled to the primary pad, the secondary pad suddenly stops switching to stop requesting power transfer.
- Phase shift pulse test: Some control schemes may introduce a slight secondary phase shift; in this test, the secondary implements a 180° phase shift during power transfer.

[4]While the system remains stable, as the carrier magnitude further increases, the increasing margin between the real axis crossing and the critical points suggests a faster transient attenuation.

TABLE 4. Simulated Test Results

Test	Primary Energy	Secondary Energy	Efficiency
Benchmark	3.66 kJ	3.53 kJ	96.60%
Standard	3.13 kJ	3.01 kJ	96.20%
Half	1.63 kJ	1.57 kJ	96.43%
Phase Shift	3.13 kJ	3.01 kJ	96.19%

C. BENCHMARK PULSE TEST

The benchmark test simulated ideal laboratory conditions, without the contributions included in this paper and therefore unsuitable for DWPT. Two key differences distinguished the benchmark test from subsequent tests. First, the primary pad remained active during the whole simulation, as it lacked a clear turn-on/turn-off signal. For such a system to be practically realizable, an additional system to detect an approaching secondary and turn on the primary is needed.

Second, the secondary system operated with passive rectification, increasing losses and decreasing total power flow. In effect, this simulation reflected a common paradigm, where the primary drives the power transfer, and the secondary responds.

The waveforms of power transferred through the primary and secondary are shown in Fig. 17(a). Note that the primary power and secondary power waveforms are nearly superimposed, with the primary power slightly higher, indicating some system losses. Power transferred and power received are included in Table 4. Generally, the pulse shape is as expected, with a linear ramp-up and a relatively flat profile during power transfer. There is an impulse as the secondary powers on, but the profile is otherwise smooth.

D. STANDARD PULSE TEST

The standard operation test simulated the expected operation of the system as described in this paper. All synchronization and detection information was transmitted solely through the induced primary inverter current. The primary and secondary power waveforms are shown in Fig. 17(b). Relevant values are shown in Table 4. With this test, a clear turn-on and turn-off transition was expected and observed. Further, the power transfer was expected to be nearly identical to that in

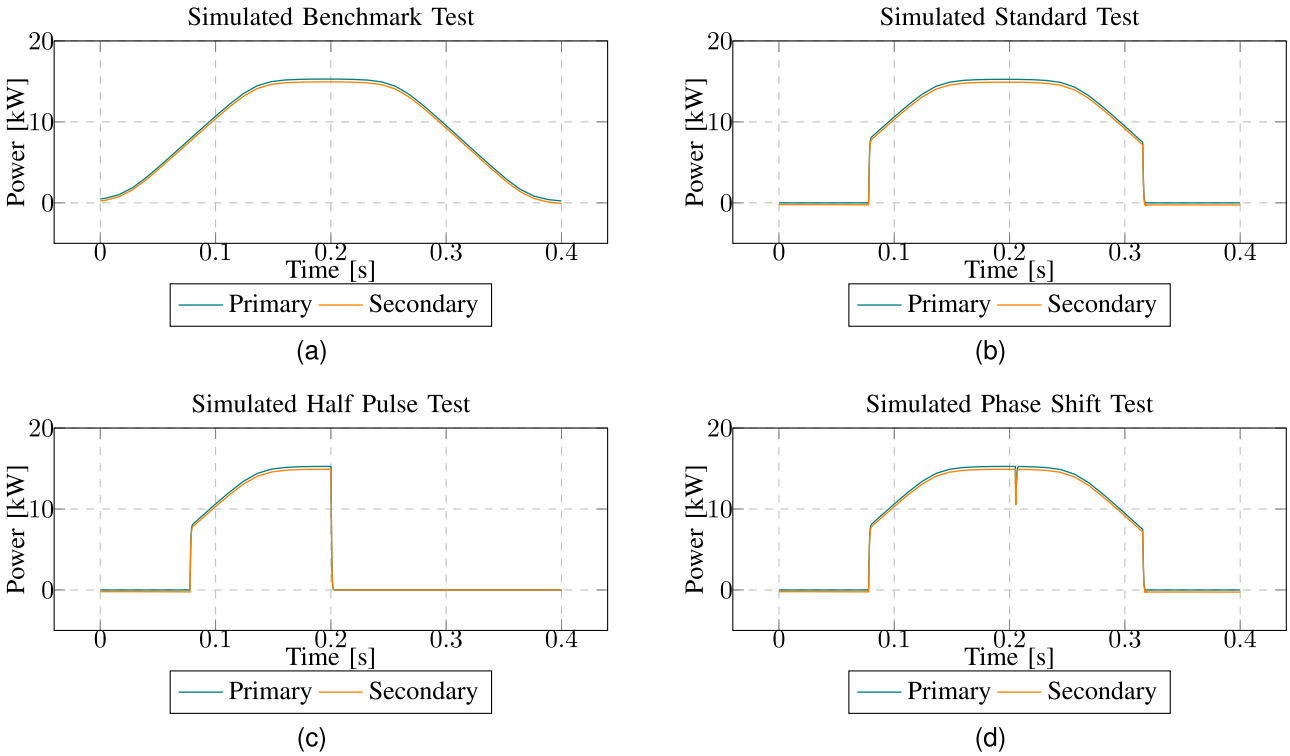

FIGURE 17. Plots of simulated primary power (blue) and secondary power (orange) for the four tests. The vertical axis is power in kilowatts; the horizontal axis, time in seconds.

the control test, as the primary remained active when the induced voltage was high enough to transfer appreciable power. Finally, as the data link is an intrinsic characteristic of the power link, the data link is as robust and reliable as the power link — a desirable effect of this system.

E. HALF PULSE TEST

The half pulse test and the phase shift test demonstrate the reliability of the control algorithm against disturbances. In the half pulse, the secondary inverter closes both low-side switches (U_{2S} and U_{4S}) and opens both high-side switches (U_{1S} and U_{3S}), forcing $v_{B,S} = 0\,\mathrm{V}$. As discussed previously, i_{1P} at f_f is proportional to $v_{B,S}$, so setting $v_{B,S} = 0\,\mathrm{V}$ should stop power transfer. This tests the response of the primary to a bang-bang secondary control scheme. When the secondary H-bridge stops commutation, we expect the $\bar{I}_{1P}$ to rapidly decay to zero, causing the primary to shut off.

As seen in Fig. 17(c), the desired operation is observed. The power transfer follows the first half of the pulse seen in Fig. 17(b). Halfway through the pulse, the power drops to 0 and the primary inverter shuts off, as expected. The total power transfer is expected to be roughly half that in the other tests, which is observed in Table 4.

F. PHASE SHIFT PULSE TEST

The third test instantaneously shifted the secondary H-bridge phase by 180°. Some control schemes introduce a small phase shift; the goal of this test is to demonstrate robustness against any phase effects that may occur, and further demonstrate that the primary will always send power to the secondary. Immediately after the phase shift, we expect the flow of power to be reversed. In a successful test, however, the primary will quickly respond and begin sending power to the secondary once again.

As seen in the power transfer plot in Fig. 17(d), the power flow direction quickly responds to the phase shift. The low-pass filter attenuates negative power flow; the total transient duration is very short. Further, the total power transferred is nearly as high as in the standard pulse test, as seen in Table 4.

G. SUMMARY

As can be seen in Table 4, no appreciable difference in efficiency exists between the benchmark test and the standard operation test, indicating that the synchronization and detection algorithm presented here works as designed, with each primary pad responding independently to the secondary pad. Further, we observe that the energy transferred during both robustness tests (half pulse and phase shift pulse) is as expected. The efficiency and power transferred vary less than 0.1% between the standard test and the phase shift test.

As discussed in Section V-B, the turn-on limit is set sufficiently high to ensure stable operation at turn-on. However, this reduces total power transfer. Without changing the power transfer system, this could be fixed by lowering the turn-on current $I_{1crit,P}$. While this would transfer power at 85 kHz for a longer interval, this would also introduce a component of

$v_{B,P}$ at one or both of the equilibrium frequencies f_{e1} and f_{e2}, increasing power ripple and potentially reducing efficiency. The designer must consider whether that instability and potential efficiency reduction, or a shorter power transfer interval, is more acceptable.

The simulated tests also show a robust primary–secondary communication link. Because all necessary information for synchronization and detection is inherent in power transfer, the communication link is established through the power link, and both share a strong degree of robustness. The standard operation and robustness tests did not require any additional, weaker communication link, such as a hard-wired connection or an optical coupler.

Finally, the simulation demonstrates that the proposed design is robust against system disturbances. Both the phase-shift pulse and the half-pulse test simulate the extremes in secondary control strategies. In both cases, the primary responds as expected, shutting off when the secondary did, or matching the secondary phase. The simulated results show comparable performance to an omniscient primary controller but with no dedicated communication link and significant robustness built into the system.

VI. HARDWARE VALIDATION

Three hardware tests were run to validate the simulated results: first, a standard test; second, a half-pulse test; and finally, a phase shift test.

This scheme was tested on an existing DWPT system, demonstrating the adaptability of the proposed approach to an arbitrary topology. As in the simulation, an analog anti-resonance filter sensed the primary inverter current to insert the appropriate phase shift. A digital filter, implemented on an FPGA, sampled the filtered, sensed, current to determine the on/off thresholds. The digital turn-on/off filter sampled the primary inverter current at 31 kHz.

Due to some hardware limitations, a few minor modifications differentiated the simulated test from the hardware tests:

- Hardware and propagation delays added some phase to the system; to counteract that lag and still achieve ZVS, the system operated at 84.25 kHz, rather than 85 kHz. ZVS, not a concern in simulation, was achieved with current harmonics, as in [30].
- To counteract some jitter in the comparator, the comparator output was not sampled for roughly 700 ns after a transition.
- The setup moved at roughly 1.5 MPH
- Due to space constraints, the secondary reversed direction over the primary pad, rather than passing over the entire pad in a continuous motion.
- To counteract noise in the envelope detector, the system did not begin switching until 25 consecutive iterations of the envelope detector indicated sufficient coupling. Likewise, the primary did not stop switching until 25 consecutive iterations of the envelope detector suggested insufficient coupling. A long buffer was necessary to counteract the relatively slow speed of the setup and some noise in the envelope detector.

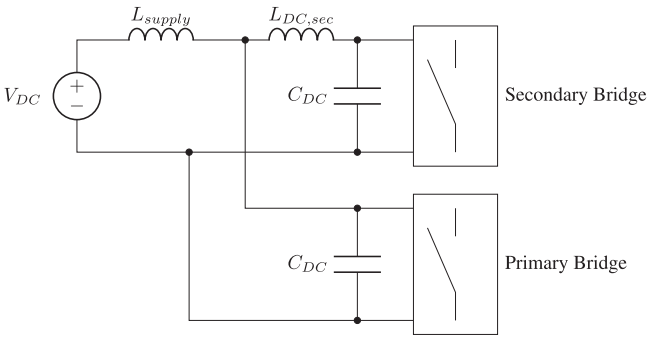

FIGURE 18. Diagram of recirculating current with bus capacitances and inductances.

TABLE 5. Experimental Component Values

Component	Value	Component	Value
$V_{DC,P}$	300 V	$V_{DC,S}$	300 V
$L_{S,P}$	5.62 µH	$L_{S,S}$	3.35 µH
$C_{P,P}$	631 nF	$C_{P,S}$	1.04 µF
$C_{C,P}$	415 nF	$C_{C,S}$	990 nF
$L_{Coil,P}$	14.2 µH	$L_{Coil,S}$	8.10 µH
$\max(M_{PS})$	1.61 µH	$\min(M_{PS})$	534 pH
$\max(M_{PP})$	−35.3 nH	$\min(M_{PP})$	−73.7 nH
L_{supply}	≈1 µH	$L_{DC,sec}$	960 µH
R_{bus}	1 mΩ	C_{DC}	200 µF

The current recirculated, with bus inductances and capacitances as in Fig. 18. The system parameters of the hardware test, on which the simulated design was based, are included in Table 5. Note that the benchmark test detailed in Section V-C assumes an unrealizable system, where the secondary and primary are perfectly synchronized. Because the simulated system is unrealizable, an experimental verification of the benchmark test is omitted.

A sample oscilloscope screen capture during power transfer is shown in Fig. 19. In that image, the inverted current shows a sharp angle when the voltage inverts; the direction of the current corner indicates inversion, rather than rectification. The setup is shown in Fig. 20.

The remainder of this section gives results for each hardware test in Sections VI-A to VI-C, with comparison in Section VI-D.

An oscilloscope screen capture of a typical turn-off transition is given in Fig. 22. Although this transition was measured at a lower power than the other experimental results, the transition is representative of all turn-off transitions.

A. STANDARD PULSE TEST

The hardware standard pulse test mirrored the simulated test described in Section V-D. The power waveforms are shown in

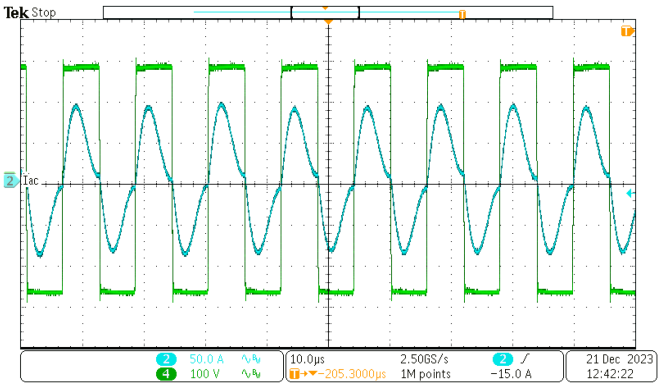

FIGURE 19. Oscilloscope screen capture of the primary side during typical operation, with voltage $v_{B,P}$ and current i_{1P} represented.

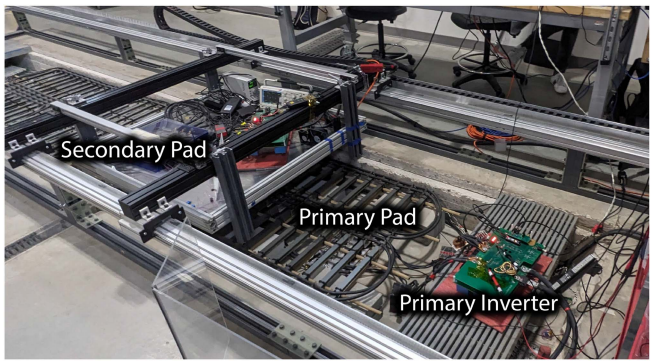

FIGURE 20. Picture of the experimental setup. The wireless power transfer coils, inverters, and control board are seen.

TABLE 6. Hardware Test Results

Test	Primary Energy	Secondary Energy	Efficiency
Standard	58.36 kJ	52.94 J	90.72%
Half	28.89 kJ	26.00 kJ	89.98%
Phase Shift	57.91 kJ	52.664 kJ	90.94%

Fig. 21(a), and the energy transferred during both consecutive pulses is shown in Table 6.

Note relatively lower efficiency and power transfer compared to the simulated results. These values could be improved with more ideal components; however, we note an effective proof of concept observed in hardware. In response to an induced current, the primary inverter switches to inject power into the system; while controlling an inverter to inject power could introduce instability, the analog and digital filters work as expected to stabilize the system. The primary only injects power at the switching frequency and turns on and off correctly as the secondary conduction angle is modulated.

B. HALF PULSE TEST

A hardware half pulse test reflected the simulation described in Section V-E. The secondary inverter operates normally through the first part of the test. Halfway through the pulse, the secondary stops switching its inverter.

The experimental results, plotted in Fig. 21(b), match the simulated results in Fig. 17(c). For the first portion of the pulse, the power transfer profile closely matches the standard simulation. However, at the midpoint of the pulse, the power drops to zero. The primary shuts off in response to the secondary inverter de-energizing the circuit, demonstrating the ideal primary response to a secondary control. There is some ringing due to the resonance of the DC system, with the DC bus capacitance and line inductance seen in Fig. 18.

C. PHASE SHIFT PULSE TEST

As in Section V-F, instantaneous phase shifts in the secondary H-bridge were introduced during power transfer. The primary and secondary power waveforms for the phase shift test, shown in Fig. 17(b), match the simulated results shown in Fig. 17(d). The total measured energy transferred during both pulses is shown in Table 6.

Note that the power transfer briefly reverses, but quickly recovers, as expected. The most critical issue is the large spike; however, this is due to the under-damped DC bus, rather than the control scheme presented here. Because the DC bus is under-damped, there is ringing with nearly a 100% overshoot. As power reverses direction, the primary and secondary DC currents overshoot, causing a large negative current. As the primary responds and the power again begins to flow in the typical direction, the currents again overshoot. The response time of the system is the delay between the downward spike and the upward spike and is typically on the order of a few cycles. Better damping on the DC bus could eliminate the overshoot, as seen in the simulated results.

The strong robustness against an instantaneous, dramatic phase shift demonstrates that the proposed system will be unaffected by any minor aberration in secondary frequency or phase. The robustness does not simply extend to the independence of each primary coil, but also to robustness against secondary aberrations. The simulated results suggest the ringing is an issue with the DC bus, and not the synchronous inversion control scheme.

D. SUMMARY

The strongest conclusion of the experimental results is the close match between the experimental and simulated results, with only minor deviations. This strong relationship suggests that any simulated design may be implemented in hardware and demonstrates that the results in Section V do not rely on timing precision or numerical precision available only in simulation.

The experimental standard operation test has some oscillation at turn-on and turn-off, which is not present in the simulated test. Even with those transients, the system performed as expected, turning on and off correctly with the primary accurately synchronizing to the secondary. The transients are due to ringing on the DC bus, where power is

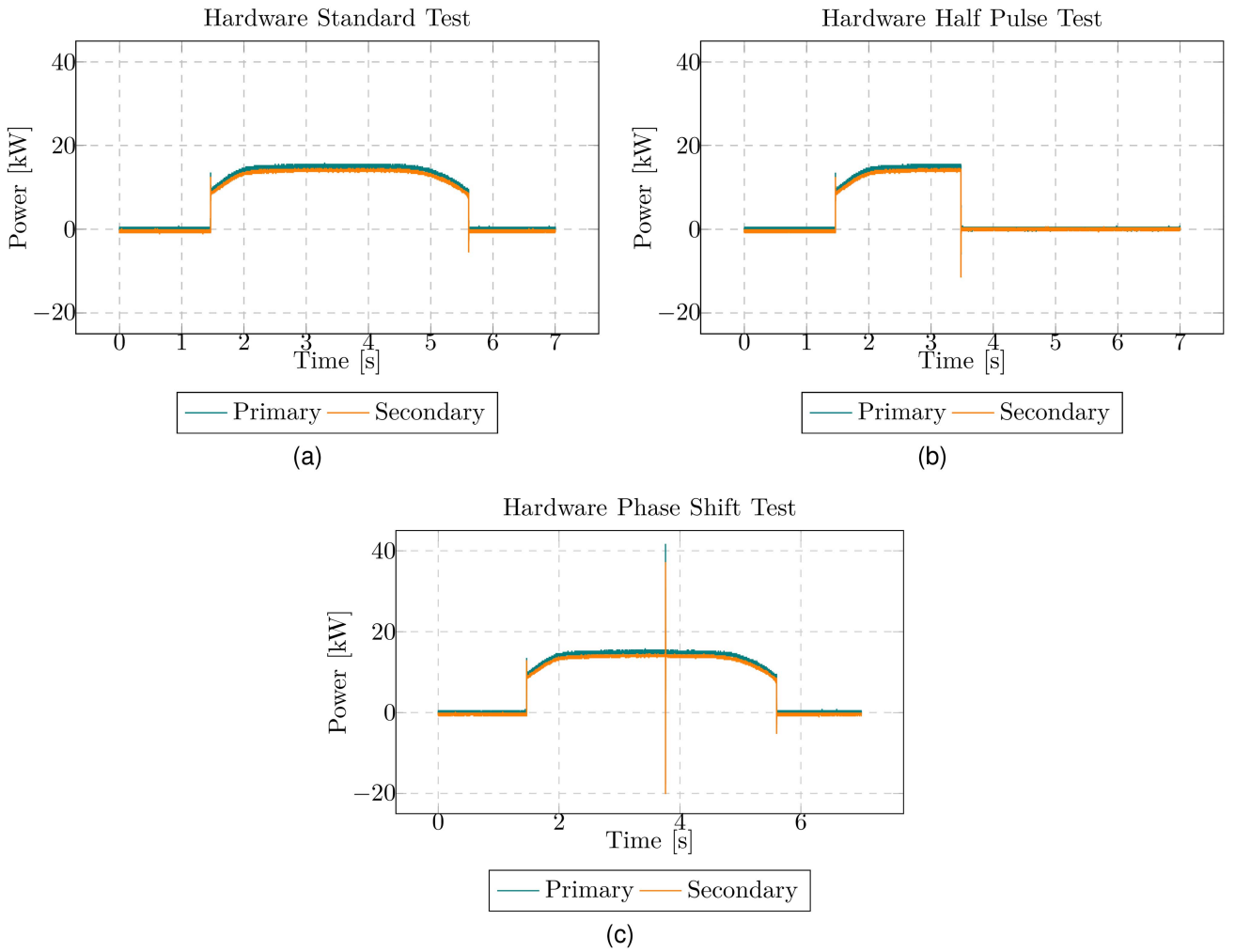

FIGURE 21. Plots of experimental primary power (blue) and secondary power (orange) for the three tests. The vertical axis is power in kilowatts; the horizontal axis, time in seconds.

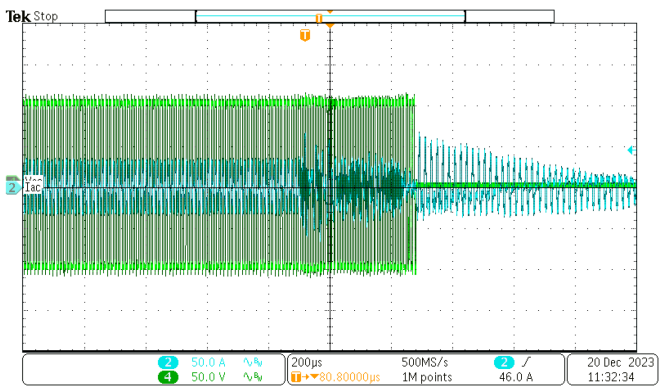

FIGURE 22. Oscilloscope screen capture of a typical turn-off transition, where $v_{B,P}$ is represented in green and i_{1P} is represented in blue. Note that for the majority of the signal, the current and voltage waveforms are regular. However, as the current signal is decreased, the system begins to operate irregularly for roughly 400 μs, before the primary shuts off. Thereafter, any remaining current is attenuated over the next 600 μs.

measured. While the overshoot is an issue for the application of this technique in its current form, the risk of that spike can be ameliorated by a properly designed and implemented EMI filter. As this paper focuses on the introduction, validation, and stability of the synchronization and detection algorithm, EMI filter design is outside the scope of the present work. Further, as discussed in Section VII, future work is presented which may further reduce the intensity of the oscillations.

With the half-pulse test, the hardware test modeled the simulation while demonstrating the efficacy and robustness of the system. When the secondary stops switching to stop requesting power transfer, the primary responds in kind and both bridges are shorted.

Finally, in the phase-shift test, the primary quickly and correctly responded to a dramatic phase shift in the secondary, demonstrating the robustness of the system to both dramatic and minor changes in the secondary phase.

VII. CONCLUSION

The approach to WPT presented here permits a variety of improvements, compared to current technologies. Those advantages are immediately applicable to DWPT scenarios, although certainly not limited to that application. The proposed approach is demonstrated in both simulation and hardware to be responsive to variations in induced primary inverter current.

The responsiveness to dynamic conditions is demonstrated by synchronization to and detection of secondary switching. The primary responds appropriately to differences in the phase and conduction angle of the secondary, demonstrating independence from any open-loop control law, and suggesting independence from a secondary closed-loop control law. Any modulations of the current induced on the primary coil by the secondary are handled well. Thus, effective operation across a range of coupling factors is similarly demonstrated.

Further, because synchronization and detection are realized over the power link, the robustness of the synchronization/detection communication link is inherently as strong as the robustness of the power link. Thus, unlike an optical coupler or a wired connection, a dual-active, secondary-driven DWPT is possible whenever any appreciable wireless power transfer is possible. That is, the proposed system is as robust as the wireless power transfer itself.

This system was developed specifically to reduce the hardware needed for realizable DWPT. The approach here presents improvements over the current state-of-the-art, in that it does not require auxiliary coils or another primary–secondary communication link, making the synchronization scheme as robust as the power transfer channel.

The single bit of information necessary for detection is transmitted by the magnitude of the induced primary inverter current, obviating the need for external hardware. Simplifying the primary-side detection to a single-bit choice places responsibility for alignment on the secondary side.

By using the synchronous inversion control scheme, both synchronization and detection are accomplished without external hardware. The benefits of a dual-active WPT system, including power regulation and lower losses, are realized without requiring any additional synchronization signal.

The main improvements of this design are as follows:

- The design simplifies the control scheme, with a single turn-on/off condition on the primary and open-loop operation on the secondary.
- The primary coils are activated by the secondary, rather than neighboring primary pads. The active switching on the secondary allows secondary power regulation and lowers semiconductor losses.
- The primary control is simplified by removing the primary clock.
- A rigorous stability criterion is established.
- Imperfectly tuned systems are addressed.
- The principle is demonstrated on a hardware system, transferring 15 kW.

Other approaches exist that can achieve some of these objectives, but no other approach allows all the above objectives to be met simultaneously and robustly. These objectives, essential for dynamic wireless power transfer, are also useful in a variety of other applications.

While this work introduces improvements over current state-of-the-art, several opportunistic for further research and development are apparent. The ringing observed in the hardware results, due to an underdamped DC bus, could also be reduced by slowly ramping up the angle between legs A and B on the primary. This could either require closing switches in some non-zero-crossing of the anti-resonance filter current, expanding the phase between the legs as the magnitude of i_{1P} increases or could require the introduction of a phase-locked loop. In either case, the next steps in the development of this approach are apparent, but beyond the scope of the current work.

Although there remains space for further advancement of this technology, the development of synchronous inversion has proven possible. With regards to dynamic wireless power transfer, the synchronous inversion technology enables increased elegance in the design and could facilitate future deployment of dynamically, wirelessly powered electric vehicles.

APPENDIX A LINEARIZATION AND QUASI-LINEARIZATION OF ZERO-CROSSING DETECTOR

Although the zero-crossing detection is nonlinear, it can be locally linearized. Consider a carrier signal g_c with amplitude A at frequency f_0, summed with some infinitesimal noise signal g_n at frequency f_1:

$$\begin{aligned} g_c(x) &= A\cos(2\pi f_0 x) \\ g_n(x) &= \epsilon\cos(2\pi f_1 x) \\ g(x) &= g_c(x) + g_n(x), \end{aligned} \tag{53}$$

where ϵ is some infinitesimally small value. The signals in (53) have corresponding Fourier decompositions

$$\begin{aligned} G_c(\xi) &= \frac{A}{2}\left(\delta(\xi - f_0) + \delta(\xi + f_0)\right) \\ G_n(\xi) &= \frac{\epsilon}{2}\left(\delta(\xi - f_1) + \delta(\xi + f_1)\right) \\ G(\xi) &= G_c(\xi) + G_n(\xi). \end{aligned} \tag{54}$$

Let the zero-crossing detection be modeled by the sign function,

$$h(g(x)) = \operatorname{sgn}(g(x)), \tag{55}$$

with values in the set $\{-1, 0, 1\}$. It is desired to determine the spectrum of $h(g(x))$, to analyze local stability.

When ϵ is sufficiently small, the only effect of the noise on the sign of $f(x)$ is some small shift in the zero crossings. Let

$$h(g(x)) = h_c(g_c(x)) + h_n(g_c(x), g_e(x)), \tag{56}$$

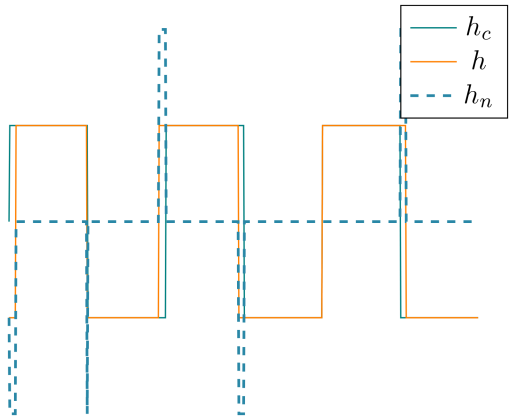

FIGURE 23. Sample figure of synchronous inversion in action. Note that the voltage commutes at the exact zero crossing, such that the sign of the voltage and current are always the same.

where h_c is a square wave, with a Fourier decomposition of

$$H_c(\xi) = \frac{2}{\pi}\left(\delta(\xi - f_0) + \delta(\xi + f_0)\right), \tag{57}$$

and $h_n(g_c(x), g_e(x))$ is some correction function, with values in the set $\{-2, 0, 2\}$. Naturally, h_c contains other harmonics, but in the linearized model, only the fundamental component is considered. The function h_n can be visualized as a series of peaks, as in Fig. 23. The Fourier transform of h^* can be calculated by

$$\int_{-\infty}^{\infty} h_n(g_c(x), g_e(x)) e^{-j2\pi\xi x} dx \tag{58}$$

It is necessary to formulate the integral in (58) as a summation of the peaks in h_n on the edges of the carrier signal $g_c(x)$. Let $\Delta_{n,f}$ be the width of the n^{th} pulse in h_n, occurring on a falling edge of $g_c(x)$; similarly, let $\Delta_{n,r}$ be the width of the n^{th} pulse in h_n, occurring on a rising edge of $g_c(x)$. The falling edges of $g_c(x)$ occur at

$$x = \frac{n + 0.25}{f_0}, \tag{59}$$

with the rising edges occurring at

$$x = \frac{n - 0.25}{f_0}, \tag{60}$$

where $n \in \mathbb{Z}$.

On the falling edges, if $\Delta_{n,f} > 0$, the value of h_n on that interval is 2. If $\Delta_{n,f} < 0$, the value of h_n on that interval is -2. Regardless of the sign of $\Delta_{n,f}$, the portion of (58) corresponding to falling edges can be expressed as

$$\sum_n \left(\int_{x=\frac{n+0.25}{f_0}}^{x=\frac{n+0.25}{f_0}+\Delta_{n,f}} 2e^{-j2\pi\xi x} dx \right). \tag{61}$$

This can also be expressed as

$$\sum_n E\left[\int_{x=\frac{n+0.25}{f_0}}^{x=\frac{n+0.25}{f_0}+\Delta_{n,f}} 2e^{-j2\pi\xi x} dx \right]. \tag{62}$$

Note that in the linearized system, we can ignore the harmonics. As will be discussed later, two frequencies are required to represent the pulses. We can replace the pulses seen in Fig. 23 with a series of sinusoids, with coefficients α_k to be determined hereafter, such that pulses are equivalently approximated by the series:

$$s(x) = \sum_k \alpha_k e^{j2\pi f_k x}, \tag{63}$$

which has the spectrum

$$\sum_k \alpha_k \delta(\xi - f_k). \tag{64}$$

In (62), the expectation is calculated over a period of the carrier signal. Over one period and neglecting harmonics, the expectation with the sinusoidal approximation can be calculated as

$$E\left[\int_{\frac{n}{f_0}}^{\frac{n1}{f_0}} s(x) e^{-j2\pi\xi x} dx \right] = \begin{cases} \frac{\alpha_k}{f_0}, & \xi = f_k \\ 0, & \text{otherwise} \end{cases} \tag{65}$$

The zero-crossing detector output spectrum, defined in (64), can be calculated by equating the expectation in (65) to the summand in (62), which will yield the values of α_1 and α_2. Combined with the definition in (64), those values produce spectrum of the zero-crossing detector output.

The balance of this appendix solves for α_1 and α_2. To that end, it is necessary to define the values $\Delta_{n,f}$; a similar process can be used to determine the values of $\Delta_{n,r}$. We solve for

$$A\cos(2\pi f_0 x) + \epsilon\cos(2\pi f_1 x) = 0$$
$$x = \frac{n + 0.25}{f_0} + \Delta_{n,f}. \tag{66}$$

It can be shown that (66) is exactly equal to

$$\begin{aligned} 0 = & -A\sin\left(2\pi f_0 \Delta_{n,f}\right) \\ & + \epsilon\cos\left(\frac{2\pi f_1 (n + 0.25)}{f_0}\right)\cos\left(2\pi f_1 \Delta_{n,f}\right) \\ & - \epsilon\sin\left(\frac{2\pi f_1 (n + 0.25)}{f_0}\right)\sin\left(2\pi f_1 \Delta_{n,f}\right) \end{aligned} \tag{67}$$

for $n \in \mathbb{Z}$. Because $\Delta_{n,f}$ is small for an infinitesimal ϵ, the small-angle approximation can be used to simplify (67) as

$$\begin{aligned} 0 = & -2A\pi f_0 \Delta_{n,f} + \epsilon\cos\left(\frac{2\pi f_1 (n + 0.25)}{f_0}\right) \\ & - \epsilon\sin\left(\frac{2\pi f_1 (n + 0.25)}{f_0}\right) 2\pi f_1 \Delta_{n,f} \end{aligned} \tag{68}$$

Noting that $|\epsilon f_1 \sin(\cdot)| \ll |f_0|$ for an infinitesimal ϵ, it is observed that (68) has an approximate solution at

$$\Delta_{n,f} = \frac{\epsilon}{A} \frac{\cos\left(\frac{2\pi f_1 (n+0.25)}{f_0}\right)}{2\pi f_0}. \tag{69}$$

Now, we can equate the summand in (62) to (65), in order to solve for α_1. and α_2. Because $\Delta_{n,f}$ is infinitesimal, the

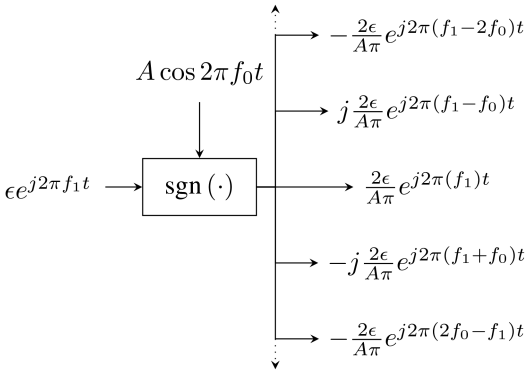

FIGURE 24. Small-signal model for a zero-crossing detector, including additional sidelobe frequencies, due to the non-linearity of the sign function. For simplicity, only 2 sidelobe frequencies are shown on each side, although an infinite number are present. Distinct paths exist for each central and sidelobe frequency. Note that a real input signal will still produce a real output signal.

Leibniz integral rule and first-order approximation reduce the summand in (62) to

$$E\left[\Delta_{n,f}2e^{-j2\pi\xi\frac{n+0.25}{f_0}}\right]. \tag{70}$$

Substituting (69) into the expression yields

$$\frac{\epsilon}{A\pi f_0}E\left[\cos\left(2\pi\frac{f_1}{f_0}(n+0.25)\right)e^{-j2\pi\xi\frac{n+0.25}{f_0}}\right]. \tag{71}$$

which expands to

$$\frac{\epsilon}{2A\pi f_0}E\left[e^{j2\pi(n+0.25)\left(\frac{f_1}{f_0}-\frac{\xi}{f_0}\right)}+e^{-j2\pi(n+0.25)\left(\frac{f_1}{f_0}+\frac{\xi}{f_0}\right)}\right]. \tag{72}$$

This reduces to

$$E\left[\Delta_{n,f}2e^{-j2\pi\xi\frac{n+0.25}{f_0}}\right]=\begin{cases}\frac{\epsilon(-j)^k}{2A\pi f_0}, & \xi=\pm f_1+kf_0, k\in\mathbb{Z}\\ 0 & \text{otherwise}\end{cases} \tag{73}$$

In assuming the pulses could be approximated by a series of sinusoids, additional frequencies were introduced. Those additional frequencies can be defined by equating (76) with (65) and substituting into (64), which yields the output spectrum

$$\sum_{k\in\mathbb{Z}}\frac{\epsilon(-j)^k}{2A\pi}\left(\delta(\xi-f_1-kf_0)+\delta(\xi+f_1-kf_0)\right). \tag{74}$$

However, (74) only considers the effects of the noise signal on the falling edges of the carrier wave; a similar effect can be shown to be effected on the rising edges of the carrier wave. Thus, the effect should be doubled to account for both effects. The quasi-linear, small-signal model of the zero-crossing detector is given by

$$H_n(\xi)=\sum_{k\in\mathbb{Z}}\left(\frac{2(-j)^k}{A\pi}G_n(\xi-kf_0)\right) \tag{75}$$

which is illustrated in Fig. 24. This can only be quasi-linear, as additional frequencies are introduced. However, accounting for these additional frequencies is essential; it is possible for an additional frequency to couple with a base frequency and increase the effective loop gain, resulting in system instability.

Although (73) includes components across an infinite spectrum of frequencies, some of the higher frequencies can be neglected if the gain of the transfer function is sufficiently low at frequencies near or above $2f_0$. In such cases, (75) can be approximated by:

$$H_n(\xi)=\sum_{k=-2}^{2}\left(\frac{2(-j)^k}{A\pi}G_n(\xi-kf_0)\right) \tag{76}$$

The fully linear system, excluding all frequencies not present in the noise spectrum, is further simplified to

$$H_n(\xi)=\frac{2}{A\pi}G_n(\xi) \tag{77}$$

APPENDIX B TIME-DOMAIN STABILITY ANALYSIS

It may be informative to verify the stability criteria developed in Section III using a time-domain analysis. Such an approach is cumbersome for developing a closed-form solution, but may function adequately as a verification of the frequency-domain stability requirements in a given system. In this appendix, the framework is developed in Appendix B, and the stability of the system described in Sections V and VI is discussed in Appendix B.

A. TIME-DOMAIN STABILITY FRAMEWORK

Traditional time-domain stability analysis uses tools such as Lyupanov functions to show that the the energy in a system perturbation decreases with time. However, in this case, such an approach is difficult at best: the switching action reactive power into the system at the switching harmonics, and energy flows into and out from the network during one switching period.

A more promising approach is to model the dynamics in a discrete-time system. The analysis is simplified by sampling the system states during the center of the pulses on $v_{B,P}$. Let the states be collected into a vector $\mathbf{x}$. The small-signal portion of $\mathbf{x}$ is given by $\hat{\mathbf{x}}$. The small-signal dynamics are linearized, and the eigenvalues of the linearized model can be used to test stability. In the discrete-time formulation, the system is stable if the eigenvalues of the linearized dynamics have length of less than 1. For convenience, the discrete time dynamics are modeled over half a switching period. Where T is the switching period $1/f_f$, we observe the small-signal dynamic relationship:

$$\begin{aligned}\hat{\mathbf{x}}\left(t+\frac{T}{2}\right)&=f_1(\hat{\mathbf{x}}(t))\\ \hat{\mathbf{x}}(t+T)&=f_2(\hat{\mathbf{x}}(t))\\ f_2(\hat{\mathbf{x}}(t))&=f_1(\hat{\mathbf{x}}(t))^2.\end{aligned} \tag{78}$$

Thus, it is sufficient to test the eigenvalues of the linearized f_1 to determine in any of the eigenvalues of f_2 exceed unity in length.

It is necessary to determine the continuous-time dynamics before developing the discrete-time system dynamics. Let A, B, and C be the state-space matrices such that

$$\dot{\mathbf{x}}(t) = A\mathbf{x}(t) + Bv_{B,P}(t) + Cv_{S,ind}(t) \tag{79}$$

where $v_{S,ind}$ is the voltage induced across $L_{Coil,P}$ by i_{2S}. Note that $v_{B,P}(t) \in \{V_{DC,P}, -V_{DC,P}\}$

Without loss of generality, reference time to the middle of the positive pulse of $v_{B,P}$. Let λ be the moment when $v_{B,P}$ switches from positive to negative.

The half-period discrete-time dynamics are given by

$$x\left(\frac{T}{2}\right) = e^{A\frac{T}{2}}x(0) + \int_0^{\lambda} e^{A\left(\frac{T}{2}-\tau\right)}BV_{DC,P} - \int_{\lambda}^{\frac{T}{2}} e^{A\left(\frac{T}{2}-\tau\right)}BV_{DC,P} + \int_0^{\frac{T}{2}} e^{A\left(\frac{T}{2}-\tau\right)}Cv_{S,ind}(t) \tag{80}$$

The expressions in (80) can be differentiated with respect to the changeable inputs:

$$\frac{\partial \mathbf{x}\left(\frac{T}{2}\right)}{\partial \mathbf{x}(0)} = e^{A\frac{T}{2}} \tag{81a}$$

$$\frac{\partial \mathbf{x}\left(\frac{T}{2}\right)}{\partial \lambda} = 2e^{A\left(\frac{T}{2}-\lambda\right)}Bv_{DC,P}, \tag{81b}$$

leading to the small-signal dynamics

$$\hat{\mathbf{x}}(\frac{T}{2}) = \frac{\partial \mathbf{x}\left(\frac{T}{2}\right)}{\partial \mathbf{x}(0)}\hat{\mathbf{x}}(0) + \frac{\partial \mathbf{x}\left(\frac{T}{2}\right)}{\partial \lambda}\hat{\lambda} \tag{82}$$

The expression in (82) indicates that the dynamics depend on both the switching moment λ and the small-signal perturbation in initial state. However, the perturbation λ is fixed by the perturbation in the initial conditions.

The states at the switching moment are given by

$$\mathbf{x}(\lambda) = e^{A\lambda}\mathbf{x}(0) + \int_0^{\lambda} e^{A(\lambda-\tau)}Bv_{DC,P}d\tau + \int_0^{\lambda} e^{A(\lambda-\tau)}Cv_{S,ind}(\tau)d\tau; \tag{83}$$

the small-signal version is approximated as

$$\hat{\mathbf{x}}(\lambda) = e^{A\lambda}\hat{\mathbf{x}}(0) + \Lambda\hat{\lambda} \tag{84}$$

where

$$\Lambda = e^{A\lambda}A\mathbf{x}(0) + Bv_{DC,P} + \int_0^{\lambda} e^{A(\lambda-\tau)}ABv_{DC,P}d\tau + Cv_{S,ind}(\lambda) + \int_0^{\lambda} e^{A(\lambda-\tau)}ACv_{S,ind}(\tau)d\tau. \tag{85}$$

Note, however, that one state is constrained to be zero at the switching moment; in the stable system, this is the output of the anti-resonance filter. Let the notation $[\cdot]_c$ refer to the row of an array or vector corresponding to the switching state. Then,

$$[\hat{\mathbf{x}}]_c = 0 = \left[e^{A\lambda}\right]_c\hat{\mathbf{x}}(0) + [\Lambda]_c\hat{\lambda}. \tag{86}$$

This yields the expression

$$\hat{\lambda} = -\frac{\left[e^{A\lambda}\right]_c}{[\Lambda]_c}\hat{\mathbf{x}}(0). \tag{87}$$

Note that Λ is a column vector, so $[\Lambda]_c$ is a scalar and the division is defined.

Substituting (87) into (82) yields the expression

$$\hat{\mathbf{x}}\left(\frac{T}{2}\right) = \left(\frac{\partial \mathbf{x}\left(\frac{T}{2}\right)}{\partial \mathbf{x}(0)} + \frac{\partial \mathbf{x}\left(\frac{T}{2}\right)}{\partial \lambda}\frac{\left[e^{A\lambda}\right]_c}{[\Lambda]_c}\right)\hat{\mathbf{x}}(0) \tag{88}$$

If all the eigenvalues of

$$\left(\frac{\partial \mathbf{x}\left(\frac{T}{2}\right)}{\partial \mathbf{x}(0)} - \frac{\partial \mathbf{x}\left(\frac{T}{2}\right)}{\partial \lambda}\frac{\left[e^{A\lambda}\right]_c}{[\Lambda]_c}\right) \tag{89}$$

lie within the complex unit circle, the system is stable.

B. STABILITY ANALYSIS OF EXAMPLE SYSTEM

Referring to the system parameters defined in Table 3, the state space model can be for an arbitrary voltage $v_{S,ind}$. In Section V, it was determined that a threshold current of 40 A was sufficient to ensure stability. Here, the eigenvalues of the matrix described in (89) are determined when the threshold current in 40 A.

First, imagine that the fourth-order filter is implemented by two cascaded parallel RLC filters. Let v_{CP} be the voltage across $C_{P,P}$ and let v_{CS} is the voltage across $C_{S,P}$. Further let $i_{f,1}$ and $v_{f,1}$ be the inductor current and capacitor voltage in the first stage, and $i_{f,2}$ and v_{f_2} be the corresponding quantities in the second stage. Because the magnitude gain of the anti-resonance filter is irrelevant, the filter inductances can be $1/\omega$, the capacitances can be $1/\omega$, and the filter resistances can be Q. The state vector is given by

$$\mathbf{x} = \begin{bmatrix} i_{1P} & i_{2P} & v_{CP} & v_{CS} & i_{filt,1} & v_{filt,1} & i_{filt,2} & v_{filt,2} \end{bmatrix}^T \tag{90}$$

and the dynamics are given in (79). The system can be simulated to determine an equilibrium point, after which the eigenvalues of the matrix expressed in (89) can be calculated. Because (89) is best calculated numerically, the it yields minimal insights. The simplest method to stabilize the synchronization and detection algorithm is to leverage the insights in Section III-C, simulate the system to arrive at a steady-state solution, and them prove stability in the time domain by determining if that the eigenvalues of (89) lie within the complex unit circle.

For the system described in Sections V and VI, with sufficient secondary-induced voltage to force $\bar{I}_{1P} = I_{1crit,P}$, the

equilibrium point is simulated to be

$$\mathbf{x} = \begin{bmatrix} 37.2\,\text{A} \\ -0.6\,\text{A} \\ 396.3\,\text{V} \\ -581.2\,\text{V} \\ -0.5\,\text{A} \\ 190.9\,\text{V} \\ -4.4\,\text{A} \\ 929.8\,\text{V} \end{bmatrix}^T \tag{91}$$

Note that the extreme voltages seen in the last elements of $\mathbf{x}$ are an artifact of the representation of a transfer function in a state-space model, and would not be present in a realized circuit. Further note that the circuit was slightly mistuned; to align the zero-crossings as expected an offset of 77 ns was introduced in the secondary-induced voltage.

Using the equilibrium values in (91), the matrix defined in (89) is found to have the eigenvalues in the set

$$\begin{aligned} \{&-0.3638 + j0.8939, \quad -0.3638 - j0.8939, \\ &-0.5153 + j0.6020, \quad -0.5153 - j0.6020, \\ &-0.7096 + j0.0000, \quad -0.7366 + j0.0000, \\ &-0.9158 + j0.2989, \quad -0.9158 - j0.2989\} \end{aligned} \tag{92}$$

The greatest norm of any of the eigenvalues is 0.9651, which lies inside the unit circle, proving time-domain stability.

For comparison, consider the same initial conditions, but ignore the anti-resonance filter; that is, cross on the zero-crossings of i_{1P}. This changes the index c in the expression of $\hat{\lambda}$. In that case, the norm of the greatest eigenvalue is 1.7795, proving instability without the anti-resonance filter.

REFERENCES

[1] B. J. Limb et al., "Economic viability and environmental impact of in-motion wireless power transfer," *IEEE Trans. Transp. Electrific.*, vol. 5, no. 1, pp. 135–146, Mar. 2019.

[2] S. N. Motapon, E. Lachance, L.-A. Dessaint, and K. Al-Haddad, "A generic cycle life model for lithium-ion batteries based on fatigue theory and equivalent cycle counting," *IEEE Open J. Ind. Electron. Soc.*, vol. 1, pp. 207–217, 2020.

[3] K. Smith, A. Saxon, M. Keyser, B. Lundstrom, Z. Cao, and A. Roc, "Life prediction model for grid-connected li-ion battery energy storage system," in *Proc. IEEE Amer. Control Conf.*, 2017, pp. 4062–4068.

[4] A. Millner, "Modeling lithium ion battery degradation in electric vehicles," in *Proc. IEEE Conf. Innov. Technol. Efficient Reliable Electricity Supply*, 2010, pp. 349–356.

[5] J. V. Barreras et al., "Evaluation of a Novel BEV concept based on fixed and swappable Li-ion battery packs," *IEEE Trans. Ind. Appl.*, vol. 52, no. 6, pp. 5073–5085, Nov./Dec. 2016.

[6] S. Manzetti and F. Mariasiu, "Electric vehicle battery technologies: From present state to future systems," *Renewable Sustain. Energy Rev.*, vol. 51, pp. 1004–1012, 2015. [Online]. Available: https://www.sciencedirect.com/science/article/pii/S1364032115006577

[7] A. Fotouhi, D. J. Auger, K. Propp, S. Longo, and M. Wild, "A review on electric vehicle battery modelling: From lithium-ion toward lithium–sulphur," *Renewable Sustain. Energy Rev.*, vol. 56, pp. 1008–1021, 2016. [Online]. Available: https://www.sciencedirect.com/science/article/pii/S1364032115013921

[8] H. Ambrose, N. Pappas, and A. Kendall, "Exploring the costs of electrification for California's transit agencies," ITS Reports 2017(03), Oct. 2017, doi: 10.7922/G2PZ570Z.

[9] N. Lutsey and M. Nicholas, "Update on electric vehicle costs in the United States through 2030," The International Council on Clean Transportation, 2019, doi: 10.13140/RG.2.2.25390.56646.

[10] A. Ahmad, M. S. Alam, and R. Chabaan, "A comprehensive review of wireless charging technologies for electric vehicles," *IEEE Trans. Transp. Electrific.*, vol. 4, no. 1, pp. 38–63, Mar. 2018.

[11] M. Hansen, A. Kamineni, and R. Zane, "Zero-crossing current detection for modular and robust dynamic wireless power transfer," in *Proc. IEEE Energy Convers. Congr. Expo.*, 2020, pp. 5207–5214.

[12] M. J. Hansen, R. A. Zane, and A. Kamineni, "Zero-crossing current detection for modular and robust dynamic wireless power transfer," U.S. Patent 11,218,026, Jan. 4, 2022.

[13] A. Kamineni, M. J. Neath, A. Zaheer, G. A. Covic, and J. T. Boys, "Interoperable EV detection for dynamic wireless charging with existing hardware and free resonance," *IEEE Trans. Transp. Electrific.*, vol. 3, no. 2, pp. 370–379, Jun. 2017.

[14] S. Li, Z. Liu, H. Zhao, L. Zhu, C. Shuai, and Z. Chen, "Wireless power transfer by electric field resonance and its application in dynamic charging," *IEEE Trans. Ind. Electron.*, vol. 63, no. 10, pp. 6602–6612, Oct. 2016.

[15] E. Abramov and M. M. Peretz, "Multi-loop control for power transfer regulation in capacitive wireless systems by means of variable matching networks," *IEEE J. Emerg. Sel. Topics Power Electron.*, vol. 8, no. 3, pp. 2095–2110, Sep. 2020.

[16] F. Lu, H. Zhang, H. Hofmann, and C. Mi, "A double-sided LCLC-compensated capacitive power transfer system for electric vehicle charging," *IEEE Trans. Power Electron.*, vol. 30, no. 11, pp. 6011–6014, Nov. 2015.

[17] J. Dai and D. C. Ludois, "A survey of wireless power transfer and a critical comparison of inductive and capacitive coupling for small gap applications," *IEEE Trans. Power Electron.*, vol. 30, no. 11, pp. 6017–6029, Nov. 2015.

[18] U. K. Madawala and D. J. Thrimawithana, "A bidirectional inductive power interface for electric vehicles in V2G systems," *IEEE Trans. Ind. Electron.*, vol. 58, no. 10, pp. 4789–4796, Oct. 2011.

[19] H. Wu, T. Mu, X. Gao, and Y. Xing, "A secondary-side phase-shift-controlled LLC resonant converter with reduced conduction loss at normal operation for hold-up time compensation application," *IEEE Trans. Power Electron.*, vol. 30, no. 10, pp. 5352–5357, Oct. 2015.

[20] G. Buja, M. Bertoluzzo, and K. N. Mude, "Design and experimentation of WPT charger for electric city car," *IEEE Trans. Ind. Electron.*, vol. 62, no. 12, pp. 7436–7447, Dec. 2015.

[21] H. Hu, T. Cai, S. Duan, X. Zhang, J. Niu, and H. Feng, "An optimal variable frequency phase shift control strategy for ZVS operation within wide power range in IPT systems," *IEEE Trans. Power Electron.*, vol. 35, no. 5, pp. 5517–5530, May 2020.

[22] X. Zhang, T. Cai, S. Duan, H. Feng, H. Hu, and J. Niu, "A harmonic-considered time domain model of LCC compensated wireless power transfer systems," in *Proc. IEEE Int. Power Electron. Application Conf. Expo.*, 2018, pp. 1–5.

[23] S. Y. Chu, X. Cui, X. Zan, and A.-T. Avestruz, "Transfer-power measurement using a non-contact method for fair and accurate metering of wireless power transfer in electric vehicles," *IEEE Trans. Power Electron.*, vol. 37, no. 2, pp. 1244–1271, Feb. 2022.

[24] J. Pries, V. P. N. Galigekere, O. C. Onar, and G.-J. Su, "A 50-kW three-phase wireless power transfer system using bipolar windings and series resonant networks for rotating magnetic fields," *IEEE Trans. Power Electron.*, vol. 35, no. 5, pp. 4500–4517, May 2020.

[25] C. Cheng et al., "Load-independent wireless power transfer system for multiple loads over a long distance," *IEEE Trans. Power Electron.*, vol. 34, no. 9, pp. 9279–9288, Sep. 2019.

[26] Y. Sakayanagi, S. Togawa, K. Konagaya, and Y. Kuwahara, "Wireless power transmission for a traveling mobility scooter," in *Proc. IEEE Wireless Power Transfer Conf.*, 2016, pp. 1–3.

[27] A. N. Azad, A. Echols, V. A. Kulyukin, R. Zane, and Z. Pantic, "Analysis, optimization, and demonstration of a vehicular detection system intended for dynamic wireless charging applications," *IEEE Trans. Transp. Electrific.*, vol. 5, no. 1, pp. 147–161, Mar. 2019.

[28] G. R. Nagendra, L. Chen, G. A. Covic, and J. T. Boys, "Detection of EVs on IPT highways," *IEEE J. Emerg. Sel. Topics Power Electron.*, vol. 2, no. 3, pp. 584–597, Sep. 2014.

[29] Z. Pantic, S. Bai, and S. M. Lukic, "ZCS *LCC*-compensated resonant inverter for inductive-power-transfer application," *IEEE Trans. Ind. Electron.*, vol. 58, no. 8, pp. 3500–3510, Aug. 2011.

[30] M. Hansen, A. Kamineni, and R. Zane, "Current harmonics dead time design method to achieve ZVS with non-linear output capacitance," in *Proc. IEEE Energy Convers. Congr. Expo.*, 2021, pp. 2189–2196.
[31] Z. Ye, M. Yang, and P.-Y. Chen, "Multi-band parity-time-symmetric wireless power transfer systems," in *Proc. IEEE Wireless Power Transfer Conf.*, 2021, pp. 1–4.
[32] J. Zhou, B. Zhang, W. Xiao, D. Qiu, and Y. Chen, "Nonlinear parity-time-symmetric model for constant efficiency wireless power transfer: Application to a drone-in-flight wireless charging platform," *IEEE Trans. Ind. Electron.*, vol. 66, no. 5, pp. 4097–4107, May 2019.
[33] Z. Hua, K. T. Chau, W. Liu, and X. Tian, "Pulse frequency modulation for parity-time-symmetric wireless power transfer system," *IEEE Trans. Magn.*, vol. 58, no. 8, Aug. 2022, Art. no. 8002005.
[34] W. Gu, D. Qiu, X. Shu, B. Zhang, W. Xiao, and Y. Chen, "A constant output capacitive wireless power transfer system based on parity-time symmetric," *IEEE Trans. Circuits Syst. II: Exp. Briefs*, vol. 70, no. 7, pp. 2585–2589, Jul. 2023.
[35] O. Yu, C. Yeh, and J. Lai, "Synchronous rectifier design considerations for solid-state transformer light-load stability," in *Proc. IEEE Asian Conf. Energy, Power Transp. Electrific.*, 2018, pp. 1–5.
[36] O. Yu, C.-S. Yeh, and J.-S. Lai, "Sequential parallel switching for drain-source synchronous rectifier efficiency and light-load stability improvement," in *Proc. IEEE Appl. Power Electron. Conf. Expo.*, 2019, pp. 463–467.
[37] M. E. V. Valkenburg, *Analog Filter Design*. Austin, TX, USA: Holt, Rinehart, and Winston, 1982.
[38] R. D. Middlebrook, "Null double injection and the extra element theorem," *IEEE Trans. Educ.*, vol. 32, no. 3, pp. 167–180, Aug. 1989.
[39] *Wireless Power Transfer for Light-Duty Plug-In/Electric Vehicles and Alignment Methodology*, SAE Standard J2954_202208, SAE International, Warrendale, PA, USA, Aug. 2022. [Online]. Available: https://www.sae.org/standards/content/j2954_202208
[40] Q. Deng et al., "Edge position detection of on-line charged vehicles with segmental wireless power supply," *IEEE Trans. Veh. Technol.*, vol. 66, no. 5, pp. 3610–3621, May 2017.
[41] P. Sukprasert, B. M. Nguyen, and H. Fujimoto, "Estimation of lateral displacement of electric vehicle to an alignment of wireless power transmitters," in *Proc. IEEE/SICE Int. Symp. Syst. Integration*, 2014, pp. 542–547.

MATTHEW J. HANSEN (Graduate Student Member, IEEE) received the B.S. (magna cum laude) and Ph.D. degrees in electrical engineering from Utah State University, Logan, UT, USA, in 2020 and 2024, respectively. As a graduate student, he was a Presidential Doctoral Research Fellow. He is currently a Senior Power Electronics Engineer with Intergalactic. His research interests include the intersection of control theory, machine learning, and wireless power transfer.

AZMEER ZAHID (Graduate Student Member, IEEE) received the B.Sc. degree in electrical engineering from the Lahore University of Management Sciences, Lahore Pakistan, in 2020. He is currently working toward the Ph.D. degree in electrical and computer engineering with Utah State University, Logan, UT, USA. His research interests include addressing the challenges and developing solutions for dynamic wireless charging systems for electric roadways, with a particular emphasis on the stability and control of these systems. His work aims to enhance the efficiency and reliability of electric vehicle charging infrastructure through effective synchronization over large air gaps.

ABHILASH KAMINENI (Member, IEEE) received the B.E. degree (Hons.) in electrical engineering and the Ph.D. degree in power electronics from The University of Auckland, Auckland, New Zealand, in 2012 and 2017, respectively. He was a Postdoctoral Fellow and an Assistant Professor with Power Electronics Laboratory, Utah State University, Logan, UT, USA, in 2017 and 2019, respectively. His research interests include wireless power transfer and resonant converters.